Clinical Biomechanics 132 (2026) 106744

Contents lists available at ScienceDirect

Clinical Biomechanics

journal homepage: www.elsevier.com/locate/clinbiomech

Original articles

A partial differential equation model of a novel treatment for chronic wound biofilm infections☆

Sandeep Shirgill [a,b,c,*], Najida Begum [f], Sarah A. Kuehne [b,d], Gowsihan Poologasundarampillai [b], Sara Jabbari [a], John Ward [e]

[a] School of Mathematics, University of Birmingham, Birmingham, West Midlands, United Kingdom
[b] School of Dentistry, University of Birmingham, Birmingham, West Midlands, United Kingdom
[c] School of Infection, Inflammation and Immunology, University of Birmingham, Birmingham, West Midlands, United Kingdom
[d] School of Science and Technology, Nottingham Trent University, Nottingham, Nottinghamshire, United Kingdom
[e] Department of Mathematical Sciences, Loughborough University, Loughborough, Leicestershire, United Kingdom
[f] FIECON, Hodgkin Huxley house, London, United Kingdom

ARTICLE INFO

Keywords:
Wound healing
Chronic wounds
Bioactive glass fibres
Mathematical model
Biofilm infections

ABSTRACT

Background: Chronic wounds, such as pressure ulcers, venous leg ulcers, and diabetic foot ulcers, present a significant healthcare challenge due to their prolonged healing times and association with biofilm infections. This study introduces a mathematical model to investigate wound healing dynamics during the proliferative stage, focusing on chronic wound conditions characterised by poor vascularisation, clotting deficiencies, cellular senescence, and bacterial biofilms.

Methods: The model examines the interactions between fibroblasts, keratinocytes, granulation tissue, nutrients, and signalling molecules under normal and impaired healing scenarios. The potential of bioactive glass fibres, doped with antimicrobial and wound healing ions, is also explored.

Findings: Model results reflect the impairment of wound healing by biofilm infections, with larger bacterial populations leading to poorer outcomes. Simulations suggest that antimicrobial ions reduce bacterial populations and improve nutrient availability, supporting fibroblast and immune cell activity. Reapplication of bioactive glass fibres enhances ion concentrations, further promoting granulation tissue formation and wound closure under certain conditions.

Interpretation: Results identify critical parameters that hinder healing in untreated wounds and demonstrate how bioactive glass fibre design can be optimised to enhance healing outcomes. This work provides a foundation for designing cost-effective treatments for chronic wounds, addressing a significant unmet clinical need.

1. Introduction

Chronic wound infections pose a significant challenge to healthcare systems worldwide, with conditions such as pressure ulcers, venous leg ulcers, and diabetic foot ulcers placing a heavy strain on resources. These wounds represent a substantial unmet clinical need and lead to considerable healthcare expenditures, with costs in the UK alone reaching an estimated £8.3 billion annually (based on 2017/2018 data), which is a 48% increase from the £5.3 billion reported in 2012/2013 (Kerr, 2011; Guest et al., 2020). This significant rise highlights the increasing financial strain wound management places on the NHS. With the increasing prevalence of diabetes and ageing populations, the incidence of chronic wounds is projected to rise (Margolis, 2013), intensifying the need for effective treatment solutions.

Chronic wounds are defined as slow or non-healing wounds, where wounds can last an average of 12–13 months, recur in up to 60%–70% of patients, lead to loss of function and decreased quality of life, and are a significant cause of morbidity (Richmond et al., 2013; Canadian Agency for Drugs and Technologies in Health, 2013). Common chronic wound characteristics include poor vascularisation thus leading to insufficient nutrients transported to the wound area, inability for wounds to clot effectively and cellular senescence, where cells are unable to respond as effectively to the wound environment and their function

☆ This article is part of a Special issue entitled: 'Wound care technologies' published in Clinical Biomechanics.

* Correspondence to: School of Infection, Inflammation and Immunology, University of Birmingham, Birmingham B15 2TT, United Kingdom.
E-mail address: s.shirgill@bham.ac.uk (S. Shirgill).

https://doi.org/10.1016/j.clinbiomech.2025.106744
Received 7 February 2025; Accepted 23 December 2025
Available online 8 January 2026

is disregulated. Another factor that hinders chronic wounds healing is the presence of a biofilm infection. Biofilms, comprising densely aggregated bacterial colonies encased in extracellular polymeric substances (EPS), are prevalent in chronic wounds, contributing to delayed healing and treatment resistance (James et al., 2008; Bowler et al., 2001; Percival et al., 2012; Metcalf and Bowler, 2013). Targeting these biofilm infections has shown promise in improving wound healing outcomes (Percival et al., 2012; Wolcott and Rhoads, 2008).

While existing therapies such as growth factors, engineered skin, and negative pressure wound therapy provide some benefit (Shankaran et al., 2013), they are often costly and only partially effective. Thus, there is a critical need for cost-efficient and highly effective alternatives.

In this context, bioactive glass (BG) fibres emerge as a promising treatment modality. Initially BG was developed to treat bone defects (Jones, 2013; Hoppe et al., 2011a). Recently, research has focused on delving into the wound healing properties of BG both *in vitro* and *in vivo* (Jones, 2013; Mao et al., 2014; Lin et al., 2012; Gao et al., 2017; Zhao et al., 2015; Naseri et al., 2017; Norris et al., 2020; Poologasundarampillai and Obata). It has been reported that BG can assist in wound healing by Zhao et al. (2015), Day (2005), Day et al. (2004), Lansdown (2002):

- promoting the proliferation and migration of fibroblasts, which can then produce granulation tissue;
- stimulating the secretion of angiogenic growth factors (such as VEGF and FGF) from fibroblasts and therefore stimulating angiogenesis itself and improving proliferation of endothelial cells;
- increasing vascularisation in tissue;
- accelerating blood clotting;
- stimulating the migration and proliferation of epidermal cells.

Therefore, BGs could potentially be a treatment for chronic wounds by utilising multiple mechanisms for wound healing. Increasing numbers of studies have shown that treatments involving BGs can effectively heal both acute and diabetic wounds in rats (Mao et al., 2014; Lin et al., 2012; Gao et al., 2017), thus highlighting their potential for treating human chronic wounds.

BGs can also be designed to release metal ions such as copper, zinc or cobalt, which have been shown to play a significant role in wound healing (Hoppe et al., 2011b). Furthermore, doping BG with metal ions such as silver, gallium or cerium, can also provide antimicrobial properties (Hoppe et al., 2011a; Wilkinson et al., 2018; Paterson et al., 2020; Zhao et al., 2015; Naseri et al., 2017; Jung et al., 2019; Kaya et al., 2018; Yu et al., 2012; Maleki et al., 2020; Łapa et al., 2019; Shirgill et al., 2023). Utilising the doping of BG fibres with ions that can promote wound healing and have antimicrobial capabilities holds potential for assisting the healing of chronic wounds.

Fig. 1 illustrates the wound healing dynamics of an acute wound, a chronic wound without treatment, and a chronic wound treated with BG fibres over comparable timescales, incorporating all variables modelled in this study. The acute wound progresses to full healing, while the untreated chronic wound remains unhealed, highlighting key differences in healing behaviour. For the chronic wound under BG fibre treatment, the fibres release wound-healing and antimicrobial ions, promoting granulation tissue formation and bacterial clearance. In a clinical context, it is assumed that once the BG fibres have fully dissolved, additional fibres are reapplied to sustain the healing process.

To gain deeper insights into the dynamics of wound healing, mathematical models have been developed. These models can be split into the type and stage of wound healing that is of interest. For example, many models focus on epidermal wound healing, where re-epithelialisation (migration of epithelial cells across tissue to form a barrier between the wound and the environment) is the key process (Sherratt and Murray, 1990). However, chronic wounds typically affect the dermal layer of skin too so models of dermal wound healing are also relevant. Models of dermal wound healing are split into two categories: the proliferative stage and the remodelling stage. However, chronic wounds are typically either stuck in the inflammation stage or in early proliferation stages, we therefore focus on modelling the proliferation stage. Models for the proliferative stage are further subcategorised depending on the key focus of the model, where models often either focus on angiogenesis or interactions between collagen and fibroblasts and their influence on healing (Pettet et al., 1996; Greenhalgh, 1998; Olsen et al., 1997; Machado et al., 2011; Vermolen and Javierre, 2012; Valero et al., 2013; Olsen et al., 1998; Dallon and Sherratt, 1998; Dallon et al., 1999, 2001; McDougall et al., 2006; Haugh, 2006; Menon et al., 2012; Dari et al., 2023). In contrast, our model takes a granulation-centric view of the proliferative stage. Rather than modelling capillary sprout dynamics or detailed collagen remodelling, we represent the production of granulation tissue as the central driver of progress: fibroblasts build granulation tissue, and the accumulating granulation implicitly supports vascularisation/perfusion thereby sustaining nutrient delivery and enabling re-epithelialisation. In this sense, granulation production acts as a surrogate for aspects of fibroblast–collagen dynamics and angiogenesis that are treated explicitly in the previously mentioned frameworks.

Our primary measure of healing success is whether the wound bed fills with granulation tissue (and is subsequently spanned by keratinocytes), rather than capillary density or collagen content. This reflects clinical practice, where a clean, granulating bed is a prerequisite for closure, and our aim to identify factors that delay this progression (impaired vascularisation/perfusion, clotting deficits, cellular senescence, and infection). Methodologically, this places the work within macroscopic, compartment-style formulations that track wound-bed variables and their interactions, as opposed to mechanochemical or sprout-resolving angiogenesis models, thus distinguishing this work from earlier modelling studies. To formulate the model we draw inspiration from the conceptual framework of the Mathematics-in-Medicine Study Group (2001) maggot-therapy report, which models the wound as interacting compartments of healthy tissue, necrotic tissue, and bacteria (in Medicine Study Group, 2001). We include ion-doped BG fibre treatment, where we focus on how doping them with antimicrobial metal ions (e.g. silver) or wound-healing metal ions (e.g. copper) can enhance treatment outcomes for chronic wounds. By simulating the effects of ion-doped BG fibres, the model provides a framework for optimising their design to enhance therapeutic efficacy. To our knowledge, this is the first study to model chronic wound treatment using ion-doped BG fibres, offering valuable insights for future research and clinical applications.

2. Factors affecting wound healing dynamics

2.1. Methods

Here, we develop a mathematical model of wound healing, focusing specifically on the proliferative stage of the healing process (Begum, 2009). The model addresses wounds involving damage to both the epidermis and dermis, representing full-thickness skin wounds. This wound type is characteristic of chronic wounds, making it a suitable foundation for modelling their healing dynamics. The primary objective of this section is to identify and analyse key factors influencing wound healing, with particular attention to their role in differentiating between acute wounds capable of healing and chronic wounds that fail to resolve.

2.1.1. Modelling assumptions

When modelling the no-treatment case, the following assumptions are made:

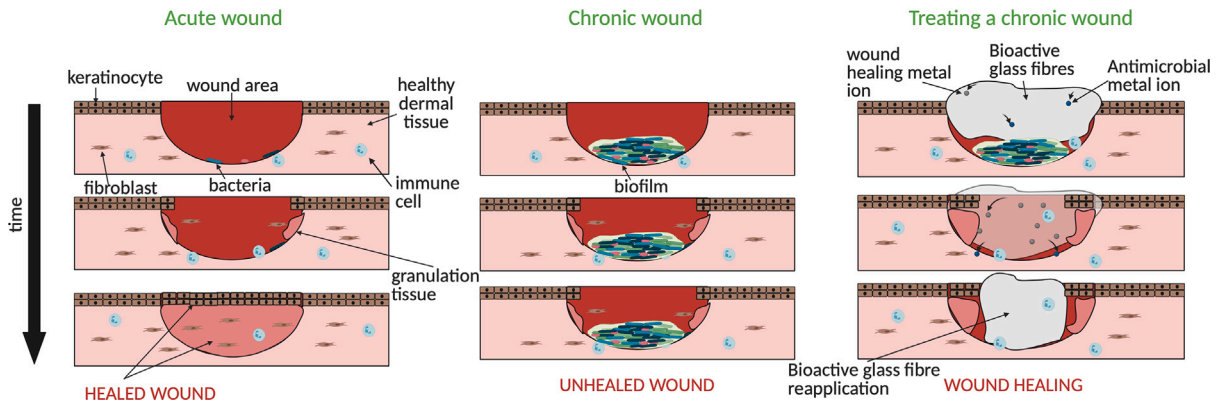

Fig. 1. Comparison of wound healing dynamics in an acute wound, a chronic wound without treatment, and a chronic wound treated with BG fibres. The acute wound heals naturally with the formation of granulation tissue and a keratinocyte layer, while the untreated chronic wound remains unhealed due to the presence of biofilm and and/or impaired wound healing mechanisms, including cellular senescence, poor clotting, and poor vascularisation. In the treated chronic wound, BG fibres release wound-healing and antimicrobial ions, promoting bacterial clearance, granulation tissue formation, and eventual wound closure. In a clinical setting, BG fibres may be reapplied once the initial fibres have dissolved to sustain the healing process. Created in BioRender.com.

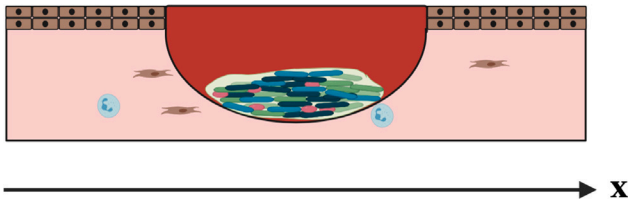

Fig. 2. A schematic representation of the modelled full-thickness wound, with all variables averaged along the wound's depth. Created using BioRender.com.

Table 1
Variable definitions from the wound healing model (1)-(8).

Variables	Description
$n(\mathbf{x},t)$	Keratinocyte cross sectional thickness
$m(\mathbf{x},t)$	Damaged dermis cross sectional thickness
$d(\mathbf{x},t)$	Healthy dermis cross sectional thickness
$g(\mathbf{x},t)$	Granulation tissue cross sectional thickness
$f(\mathbf{x},t)$	Fibroblast and immune cell cross sectional density
$c(\mathbf{x},t)$	Nutrient cross sectional concentration
$w(\mathbf{x},t)$	Bacterial cross sectional density
$s(\mathbf{x},t)$	Signal cross sectional concentration

- **Signalling molecules**: Damaged tissue releases signalling molecules (production terms in Eq. (8)), including growth factors, cytokines, and chemokines, that stimulate cell proliferation, migration, and differentiation (Traversa and Sussman, 2001). In this study, the term "signalling molecule" collectively refers to these factors, which diffuse through the wound environment (modelled by the diffusion term in Eq. (8)) and orchestrate the healing process.
- **Nutrient supply**: Generic nutrients are provided by healthy dermal tissue and granulation tissue (modelled by vasculature function in Eq. (6)), as these support the vasculature (Alhajj and Goyal, 2020).
- **Cell migration and function**: Fibroblasts, immune cells, and keratinocytes migrate from healthy tissue into the wound via diffusion and chemotaxis (migration terms in Eqs. (1) and (5)), following signalling molecule gradients (Simpson et al., 2017; Vesperini et al., 2021; Tomasova et al., 2019). These cells consume nutrients (consumption term in Eq. (6)) to sustain proliferation (growth terms in Eqs. (1) and (5)) and actively produce signalling molecules (Barrientos et al., 2008; Arango Duque and Descoteaux, 2014), with production rates increasing sharply when nutrient levels drop below a baseline threshold (Barrientos et al., 2008) (production terms in Eq. (8)).
  - **Fibroblasts**: Produce granulation tissue (production term in Eq. (4)), replacing the initial fibrin clot formed to stop bleeding (Alhajj and Goyal, 2020).
  - **Immune cells**: Clear damaged tissue and kill bacteria present in the wound (degradation terms and death terms in Eqs. (2) and (7)) (Raziyeva et al., 2021).
  - **Keratinocytes**: Responsible for re-epithelialisation (Eq. (1)) (Rousselle et al., 2019). Wound closure and the end of the proliferative phase occur when keratinocytes fully span the wound area.
- **Cell representation**: All cells involved in healing and infection clearance within the dermis are represented by a single variable, $f(\mathbf{x},t)$ (see Eq. (5)). For simplicity, this is referred to as fibroblasts and immune cells, as these are the main cell types responsible for granulation tissue formation, signalling, and infection control during healing.
- **Blood supply**: Blood supply and wound perfusion are implicitly represented by a term dependent on dermal and granulation tissue levels, accounting for the dermal health needed to support vasculature and angiogenesis (function provided in Eq. (9)). The wound is assumed to be sufficiently damaged and lacking direct blood supply, so fibroblasts and immune cells primarily migrate from the wound edge rather than arriving via a blood supply within the wound.
- **Infection dynamics**: Wound infection is represented by a single generic bacterial species (Eq. (7)) that infiltrates the wound via gaps in the keratinocyte layer. This infection inhibits wound recovery by consuming nutrients and damaging healthy dermal tissue, granulation tissue, and the keratinocyte layer (consumption and degradation/death terms in Eqs. (1), (3), (4) and (6)) (Doorbar et al., 2021; Maheswary et al., 2021; Stevens and Bryant, 2017). Bacteria can die naturally or are removed by immune cells (death terms in Eq. (7)) (MacLeod and Mansbridge, 2016).

2.1.2. Model formulation

Using the assumptions outlined in Section 2.1.1 we formulate a system of coupled non-linear partial differential equations for the variables listed in Table 1. We note these variables represent the cross-sectional densities of the species and thus are dependent on time, t, and the spatial position in the horizontal plane of the wound, coordinate (x, y) in general (Fig. 2 depicts the modelled full-thickness wound). The full dimensional model is presented in Appendix A (with parameter

definitions and units provided in Table 9) and the Eqs. (1)–(8) listed below are the dimensionless versions used in the analysis to follow.

$$\begin{aligned}\frac{\partial n}{\partial t} &= \underbrace{\nabla\cdot\left(\nabla n\right)}_{\text{Diffusion}} - \underbrace{\nabla\cdot\left(n\chi_n(d+\sigma_n g)\nabla s\right)}_{\text{Chemotaxis}} + \underbrace{\frac{c}{1+s/\gamma_{ncs}}n\left(1-\frac{n}{\kappa_n}\right)}_{\text{Birth}} \\ &\quad \underbrace{-n\left(\frac{\delta_{nc}}{1+c/\gamma_{nc}}+w\right)}_{\text{Death}},\end{aligned} \tag{1}$$

$$\frac{\partial m}{\partial t} = \underbrace{w(\beta_{nm}n+\beta_{gm}g+\beta_{dm}d)}_{\text{Production}} - \underbrace{mf(\delta_{mf}+\delta_{ms}s)}_{\text{Degradation}} - \underbrace{\delta_m m}_{\text{Natural Loss}}, \tag{2}$$

$$\frac{\partial d}{\partial t} = \underbrace{-\alpha_{dmw}wd}_{\text{Degradation}}, \tag{3}$$

$$\frac{\partial g}{\partial t} = \underbrace{\frac{cf(\beta_{gf}+\beta_{gs}s)}{1+w/\gamma_{gw}}H(s-\bar{s})H(\bar{c}-c)}_{\text{Production}} - \underbrace{g\left(\frac{\delta_{gc}}{1+c/\gamma_{gf}}+\alpha_{gmw}w\right)}_{\text{Degradation}}, \tag{4}$$

$$\begin{aligned}\frac{\partial f}{\partial t} &= \underbrace{\nabla\cdot\left(D_f\nabla f\right)}_{\text{Diffusion}} - \underbrace{\nabla\cdot\left(f\chi_f(d+\sigma_f g)\nabla s\right)}_{\text{Chemotaxis}} + \underbrace{\beta_{fb}k(d,g)}_{\text{Vasculature function}} \\ &\quad \underbrace{+f\left(\beta_{fc}c\left(1-\frac{f}{\kappa_f}\right)+\beta_{fcs}cH(s-\bar{s})\right)}_{\text{Growth}} \\ &\quad \underbrace{-f\left(\frac{\delta_{fc}}{1+(c+\rho_f s)/\gamma_{fcs}}+\alpha_{fmw}w\right)}_{\text{Death}},\end{aligned} \tag{5}$$

$$\frac{\partial c}{\partial t} = \underbrace{\nabla\cdot\left(D_c\nabla c\right)}_{\text{Diffusion}} + \underbrace{\beta_{cb}k(d,g)}_{\text{Vasculature function}} - \underbrace{c(\delta_{cn}n+\delta_{cf}f+\alpha_{cmw}w)}_{\text{Consumption}}, \tag{6}$$

$$\frac{\partial w}{\partial t} = \underbrace{w(\beta_{wc}c+\beta_{wm}m)}_{\text{Growth}} + \underbrace{\beta_{wn}H(\bar{n}-n)}_{\text{Infiltration}} - \underbrace{w(\delta_w+\delta_{wf}f)}_{\text{Death}}, \tag{7}$$

$$\begin{aligned}\frac{\partial s}{\partial t} &= \underbrace{\nabla\cdot\left(D_s\nabla s\right)}_{\text{Diffusion}} + \underbrace{\left(n(\beta_{sn}+\beta_{ssn}s)+f(\beta_{sf}+\beta_{ssf}s)\right)(1+\beta_{sc}H(\bar{c}-c))}_{\text{Production by keratinocytes and fibroblasts}} \\ &\quad + \underbrace{\beta_{sm}m+\beta_{sw}fw}_{\text{Additional production}} \underbrace{-s(\delta_s+\delta_{sn}n+\delta_{sf}f)}_{\text{Decay and cell usage}},\end{aligned} \tag{8}$$

where $H(z)$ is the Heaviside function, so that $H(z)=0$ for $z\le 0$ and $H(z)=1$ for $z>0$. We note the preference to use the dimensionless form of the model in our analysis is due to the limitation in the availability of data: most of the parameters cannot be calculated directly, but some of their ratios can be determined and are used in the rescaled equations. Here, $t=1$ is estimated to be about 7 h and a distance $x=1$ is about 0.6 mm (see Appendix C). The boundary and initial conditions are discussed in Section 2.1.3.

The formulation of the terms in the model are discussed in more detail in Appendix A, but we highlight the following key features. The Heaviside functions enable us to define a healed state:

- $n > \bar{n}$ means that the wound is sufficiently closed to prevent bacterial infection,
- leading to a recovered state with sufficient nutrient ($c > \bar{c}$),
- and reduced signalling molecule ($s < \bar{s}$),
- $s \ge \bar{s}$ activates the fibroblasts and immune cells to replicate and the former to produce granulation tissue.

The parameter scalings for non-dimensionalisation are such that healthy skin is given by $n=d=f=c=s=1$ and $m=g=w=0$. A key factor in the healing process is the local health of the blood supply, which is assumed dependent on the total amount of dermal and granulation tissue present, whereby the angiogenic processes are assumed to be fast compared to the wound healing process. The blood supply, and hence source of nutrients, is represented by the function

Table 2
Non-dimensional initial conditions (ICs) and boundary conditions (BCs) for the no-treatment model (1)–(8). Subtable (a) lists ICs and Dirichlet BCs for variables; subtable (b) lists Neumann (no-flux) BCs for derivatives at the symmetry boundary $x=0$.

(a) Variables: ICs and BCs at $x=L$ (Dirichlet).

Variable	IC ($x\in[0,L_w]$)	IC ($x\in(L_w,L]$)	BC ($x=L$)
n	0	1	1
m	1	0	–
d	0.2	1	–
g	0	0	–
f	0	1	1
c	0	1	1
w	w_0	0	–
s	0	1	1

(b) Neumann/no-flux conditions at $x=0$.

Quantity	BC ($x=0$)
n_x	0
f_x	0
c_x	0
s_x	0

Notes: (i) A dash "–" indicates no Dirichlet BC is imposed at $x=L$ for that variable. (ii) Due to symmetry/no-flux at $x=0$, we impose homogeneous Neumann conditions on n,f,c,s. Since $s_x=0$ at the boundary, the chemotactic no-flux condition reduces to the Neumann form for n and f.

$$k(d(x,t),g(x,t)) = \frac{(d+\rho_b g)^\eta}{\gamma_b^\eta+(d+\rho_b g)^\eta}, \tag{9}$$

which is an increasing function of d and g, but decreasing in constant γ_b; here, increasing the constant γ_b has the effect of reducing the effectiveness of the neo-vasculature, impeding the healing process. As well as migrating via diffusion, fibroblasts/immune cells and keratinocytes migrate chemotactically up signal molecule gradients, promoted by dermal/granular material that acts as scaffold for cell motion.

2.1.3. Modelling a one-dimensional wound

For this study, we will examine a simplified scenario, focusing on one-dimensional Cartesian geometry, with symmetry about $x=0$. We examine a patch of skin $0\le x\le L$, consisting of a wound region $0\le x\le L_w$ surrounded by healthy skin in $L_w<x\le L$. Table 2 lists the initial and boundary conditions used in the analysis, describing a long, rectangular wound for which healing will be represented by the migration of keratinocytes towards $x=0$. Due to the symmetry about $x=0$, we impose no-flux conditions for all relevant variables ($s_x=c_x=0$), which causes the chemotactic flux terms to vanish; thus, the no-flux conditions for n and f reduce to homogeneous Neumann conditions ($n_x=f_x=0$). The full-thickness wound is characterised by having no keratinocytes ($n=0$), and the presence of damaged dermal material, including clotting and eschar, henceforth referred to as "dead material" ($m>0$), and bacteria $w>0$.

The model was solved numerically in MATLAB using finite difference schemes. In particular, central difference schemes, using half-point formula for the fluxes, are applied to the diffusion and chemotaxis term and the time stepping is undertaken using a forward Euler method. Full details of numerical scheme can be found in Shirgill (2024).

2.2. Results

Firstly, we investigate interactions between variables during acute wound healing. Here, a wound exists if there is insufficient healthy dermal tissue and there is no keratinocyte layer (i.e. $d(x,t)<1$ and $n(x,t)=0$). In all simulations we set the wound to be of width $L_w=25$ (i.e. around 3 cm across) and $L=40$ (i.e. the boundary is sufficiently

Table 3
Default non-dimensional parameter values for modelling an acute wound in the system of Eqs. (1)-(8). Parameter values were determined from literature where possible (McDougall et al., 2006; Haugh, 2006; Franks et al., 2008; Schugart et al., 2008; Cai et al., 2007; Casciari et al., 1992; Waugh and Sherratt, 2006; Lauffenburger and Kennedy, 1983) or determined to produce qualitatively desirable behaviour. See Begum (2009) for more details.

Parameter	Value	Parameter	Value	Parameter	Value
γ_b	0.6	β_{sm}	6	γ_{gw}	0.5
χ_n	0.001	β_{fb}	0.04	β_{sf}	0.8
σ_n	1	δ_{sn}	0.4	$\bar{c}$	0.3
γ_{ncs}	1	δ_{sf}	0.4	γ_{gf}	0.1
κ_n	1.2	δ_s	0.64	α_{dmw}	0.1
γ_{nc}	1	η	10	α_{gmw}	0.1
δ_{nc}	0.167	β_{fc}	0.8	α_{fmw}	0.01
δ_{mf}	0.2	β_{ssf}	0.2	α_{cmw}	0.4
δ_{ms}	0.02	κ_f	1.143	β_{ghf}	0
δ_m	0	β_{fcs}	3	β_{wc}	0.2
β_{gs}	0.16	γ_{fcs}	1	β_{wm}	0.2
δ_{gc}	0	δ_{fc}	0.4	β_{wn}	0
β_{gf}	0.12	ρ_f	1	β_{sw}	0.4
$\bar{s}$	3	D_c	1.5	δ_w	0.2
β_{sc}	0.4	β_{cb}	1	δ_{wf}	0.2
D_n	1	δ_{cn}	0.236	β_{mn}	0.004
D_f	0.5	δ_{cf}	0.6	β_{mg}	0.004
χ_f	0.01	D_s	1.5	β_{md}	0.04
σ_f	1	β_{sn}	0.24	$\bar{n}$	0.5
ρ_b	0.6	β_{ssn}	0.2	δ_{nw}	1
L	40	L_w	25		

far from the wound edge to not interfere with the solutions within the wound). Table 3 presents the default set of parameter values applied for the "normal acute wound healing case" (where parameter values are determined from literature where possible or to produce qualitatively desirable behaviour, see Begum (2009) for more detail) and will be discussed in Section 2.2.1. We then focus on the effects of

- γ_b (nutrient delivery to the wound, i.e. the extent and efficiency of the vascularisation),
- β_{sm} (quality and extent of clot formation),
- β_{fcs} (cellular function of fibroblasts and immune cells),

and how these parameters can transform wound healing from an acute to chronic state. Finally, we explore the impact of bacterial infections on wound healing and their role in driving the transition from an acute to chronic state.

2.2.1. Acute wound healing without bacterial infection

We initially investigate acute wound healing in the absence of a bacterial infection ($w(x,t) = 0$). Fig. 3 shows model solutions for a successfully healed wound using the standard parameter set given in Table 3. The results display intermediate-timescale travelling-wave-like profiles with boundary effects, moving right to left from healthy (repaired/uninjured) at $x = 40$ to unhealthy (injured) skin at $x = 0$. The evolution of the signalling molecule concentration profile is shown in Fig. 3(a), demonstrating a retreating front towards $x = 0$ of elevated s within the wound. The increase in signal concentration levels exceeds the threshold seen in normal skin, and initiates the wound healing cascade of events by recruiting fibroblasts/immune cells to the affected area (Fig. 3(b)), which in turn lays down granulation tissue (Fig. 3(c)). Here the recruitment of fibroblasts/immune cells in Fig. 3(b) is from the healthy surrounding tissue, thus generating a chemotactic peak at the edge of the wound.

From Fig. 3(c), it is observed granulation tissue produced by fibroblasts/immune cells is consistent in the wound medium and ultimately fills the wound space but is raised at the wound edge, where $x = 25$. The wound edge is expected to harden during and after repair in a "real" wound, which will eventually contract and return to normal skin level with time. The non uniformity of the granulation tissue is interesting, and perhaps one of the reasons why the remodelling process in the maturation phase can lead to scar tissue formation. This behaviour was not incorporated into the model explicitly, but is predicted naturally as a model solution.

From Figs. 3(d) and 3(e), wound recovery is achieved when the vasculature supplies 80% of the nutrients typically provided to healthy tissue, and the wound domain satisfies the condition $(d + \rho_b g) > \gamma_b = 0.6$. This indicates successful revascularisation as granulation and dermal tissue are adequate to support successful angiogenesis to resupply nutrients for healing to take place (see Fig. 3(c)). It should be noted that there is a noticeable dip in $k(x,t)$ at $x \approx 25$ (see Fig. 3(d)) due to a very localised region with $c > \bar{c}$ (see Eq. (4)) so that no $g(x,t)$ is being laid down there; the incorporation of the remodelling process would perhaps remove this artefact, but nutrient diffusion from the surrounding healthy and granulation tissue and ensures that this artefact has no influence on the key results and a rectification was not pursued.

Keratinocytes are responsible for re-epithelialisation and cells migrate from the wound edges, as shown in Fig. 3(f) over a domain that has adequate nutrient and granulation tissue levels. Consequently the whole wound is eventually covered by the epidermis, enabling the wound to progress to the maturation phase and restore the skin's barrier.

As normal healing persists, Fig. 3(g) shows that the damaged dermis retreats, being replaced by granulation tissue and eventually the epidermis as shown in Figs. 3(c) and 3(f). In this simulation the revascularisation and nutrient supply within the healed domain are slightly lower than that of the healthy skin. There is paucity of quantitative data in the literature, regarding whether the levels in a healing wound should be above or below that of healthy skin, though it is straightforward to change the predicted nutrient supply by appropriately adjusting parameters γ_b and ρ_b.

We observe that dermal recovery and wound closure are obtained where the wound fills with granulation tissue by $t \approx 14$ days and re-epithelialization is completed within $t \approx 20$ days. This accounts for repair from initial damage to wound coverage, replacing dermal and epidermal tissue in the normal healing domain, for a full-thickness wound. The healed wound is close to homeostatic levels of keratinocytes, nutrients, fibroblasts/immune cells and signal levels. Adequate nutrient supply is obviously a key factor and effective to ensure skin homeostasis and complete wound repair. The effects of a less efficient blood supply are explored next.

2.2.2. A chronic wound case without infection

Adequate nutrient supply is essential for maintaining skin homeostasis and enabling complete wound repair. When blood supply is less efficient, this balance is disrupted through a combination of vascular inefficiency, impaired clotting, and cellular senescence. These mechanisms form the focus of this section.

Vascular efficiency

In Fig. 4 we increase the vascular hill function parameter to $\gamma_b = 0.85$ from $\gamma_b = 0.6$ (used in Fig. 3); this represents a reduction in vascular effectiveness in delivering nutrients and reflects the circumstances of chronic conditions such as diabetes, where nutrient supply is severely impaired as a result of poor circulation (Pastar et al., 2024).

The healing process is initially similar to the healthy equivalent (Fig. 3) but decelerates and tends to an unhealed steady state, indicated by the lack of wound closure in Fig. 4(c). Despite initially comparable signal levels (Fig. 4(a)) within the wound to Fig. 3(a) produced by the dead material and dispersing into a large proportion of the injured medium, other dermal components are unable to sustain this supply. Consequently, signal levels eventually drop below the activation threshold of $\bar{s} = 3$ leading to reduced proliferation of fibroblasts and immune cells and stalled production of granulation tissue.

Fibroblast/immune cell levels at the edge of the wound are initially high (Fig. 4(b)), however insufficient granulation tissue is laid down to

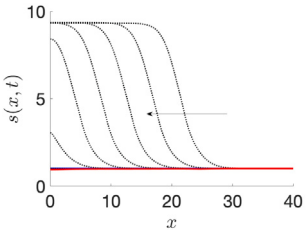

(a) Signal concentration ($s(x,t)$).

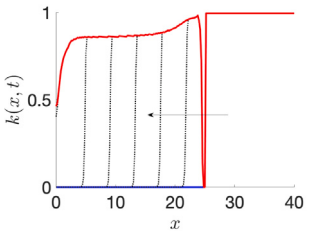

(d) Vasculature ($k(x,t)$).

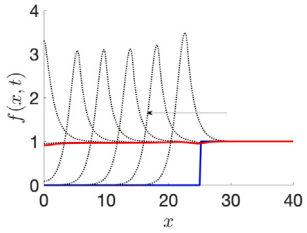

(b) Fibroblast and immune cell density ($f(x,t)$).

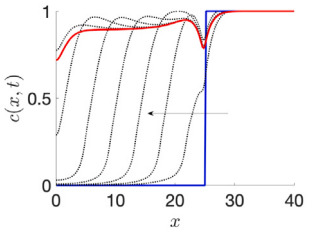

(e) Nutrient concentration ($c(x,t)$).

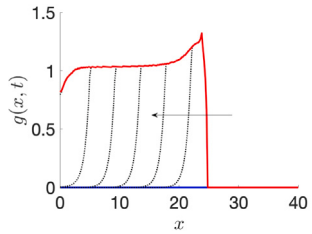

(c) Granulation tissue thickness ($g(x,t)$).

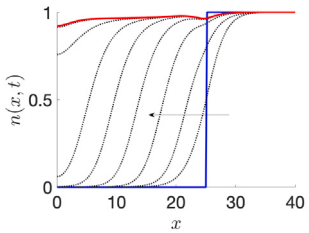

(f) Keratinocyte thickness ($n(x,t)$).

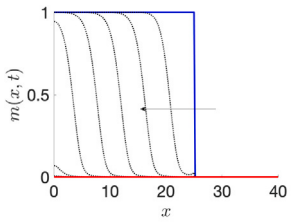

(g) Damaged dermis thickness ($m(x,t)$).

Fig. 3. Numerical solutions for (1)–(8) with ICs and BCs in Table 2, for the case of no bacterial infection (i.e. $w_0 = 0$). Solutions are shown in time steps of $t = 8$, using parameter values from Table 3. Arrows indicate the direction of variable changes over time, with the blue line representing the initial condition and the red line representing the steady-state solution. (For interpretation of the references to colour in this figure legend, the reader is referred to the web version of this article.)

support a functioning vasculature (Figs. 4(c) and 4(d)). Consequently inadequate nutrients infiltrate the wound (Fig. 4(e)), which disallows cell activity, migration, tissue growth and signal usage beyond the localised wound edge within the region of $x \in (15, 25)$, as the cells are unable to function normally or recruit further reinforcements to the wound area (Figs. 4(f) and 4(c)). In this case, damaged dermal material does not decay naturally, and hence remains in the unhealed part of the wound, there being insufficient nutrients for fibroblasts/immune cells to penetrate and degrade it (Fig. 4(e)).

Impaired clotting and cellular senescence

The clotting mechanism is crucial during the initial stages of injury, forming a protective barrier that prevents further damage and facilitates healing beneath. Inefficiencies in the clotting matrix can disrupt wound healing, providing a poor foundation for wound bed preparation and potentially inhibiting critical dermal and epidermal processes during the proliferative stage. Abnormalities in clotting are often observed in chronic wounds. Additionally, cellular senescence is another key feature of chronic wounds that significantly contributes to delayed healing. In Fig. 5, the left panels indicate poor clotting, where we reduce β_{sm} to $\beta_{sm} = 4$ (from $\beta_{sm} = 6$), and the right panels cellular senescence, where we reduce β_{fcs} to $\beta_{fcs} = 1$ (from $\beta_{fcs} = 3$); all other parameters are taken from Table 3.

When considering poor clotting, the reduction in the signalling molecule production in the wound environment (captured by the reduction in β_{sm}) results in the signal levels (Fig. 5(a)) being approximately two thirds (here $s \approx 6.2$) of that seen in the normal healing case (Fig. 3(a)), and thus cannot suffuse the whole wound to sufficient levels

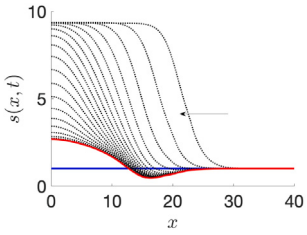

(a) Signal concentration ($s(x,t)$).

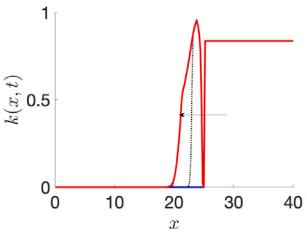

(d) Vasculature ($k(x,t)$).

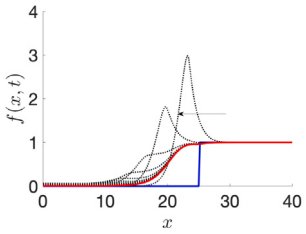

(b) Fibroblast and immune cell density ($f(x,t)$).

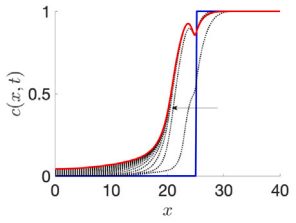

(e) Nutrient concentration ($c(x,t)$).

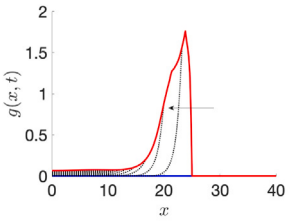

(c) Granulation tissue thickness ($g(x,t)$).

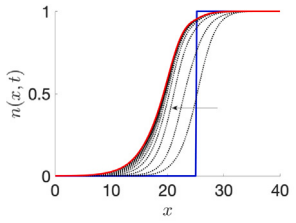

(f) Keratinocyte thickness ($n(x,t)$).

Fig. 4. Numerical solutions for (1)–(8) with ICs and BCs in Table 2, for the case of no bacterial infection (i.e. $w_0 = 0$). Solutions are shown in time steps of $t = 8$, using parameter values from Table 3 except for $\gamma_b = 0.85$. Arrows indicate the direction of variable changes over time, with the blue line representing the initial condition and the red line representing the steady-state solution. (For interpretation of the references to colour in this figure legend, the reader is referred to the web version of this article.)

for successful cell recruitment (fibroblasts/immune cells), or initiate clotting processes beyond $x \approx 15$ adequately (Figs. 5(b) and 5(c)). This results in reduced keratinocyte production and consequently no keratinocyte production occurs in the wound centre (Fig. 5(d)).

When senescent cells are present, the signalling molecule concentration is similar to that seen in acute wound healing (comparing 5(e) with 3(a)). However, the simulation reveals significantly lower fibroblast and immune cell densities compared to normal acute wound healing, as shown in Fig. 5(f) (contrast with Fig. 3(b)). This deficiency leads to reduced granulation tissue production (Fig. 5(g)), with $g(x,t) \approx 0.8$ in the central region ($x \in (5, 20)$). The reduced granulation tissue hinders adequate vasculature formation, thereby limiting nutrient supply to the wound environment. This nutrient deficiency exacerbates the decline in fibroblast and immune cell densities, creating a positive feedback loop that further impairs healing. As a result, the wound exhibits incomplete closure, with reduced granulation tissue thickness and keratinocyte proliferation, particularly at the wound centre (Figs. 5(g) and 5(h)). While healing processes are evident throughout the wound, they occur at insufficient levels to achieve full recovery.

The profiles for poor clotting closely resemble those observed under conditions of reduced nutrient delivery (γ_b=0.85) shown in Fig. 4. In contrast, cellular senescence has a comparatively weaker impact on wound healing under these parameter values. Nevertheless, all three cases demonstrate a failure in granulation tissue closure and epidermal recovery, highlighting their detrimental effects on wound healing, underscoring their critical roles in the wound healing process.

2.2.3. *Effect of bacterial infections on wound healing*

Once damaged skin is exposed to the external environment, it will naturally come into contact with micro-organisms such as the bacteria, including *Staphylococcus aureus*, *Streptococcus spp* and *Pseudomonas aeruginosa* (Puca et al., 2021). Deep wound tissue provides an ideal habitat for bacterial invasion. If left unchecked, this may impair wound bed preparation and contribute to chronic wound development (Maheswary et al., 2021). Many species of infecting bacteria metabolise nutrients both aerobically and anaerobically, with the ability to adapt to hypoxic conditions resulting in overabundant bacterial burden or critical colonisation in the affected area (Guo et al., 2022). Invasion can delay the healing process and is a major cause of wounds becoming chronic rather than acute (Cavallo et al., 2024). Here, the role of bacterial infections in wound healing is investigated.

Fig. 6 presents simulations using the same parameter values as the healing wound case in Fig. 2, except for an initial bacterial load of $w(x,0) = w_0 > 0$ in the wound region $x \in [0, L_w]$. We compare inocula of $w_0 = 0.05$ (left panels) and $w_0 = 0.5$ (right panels) at the initial wound site. With the low inoculum, $w_0 = 0.05$, it can be observed that healing is successful as bacteria retreat (Fig. 6(a)). A higher inoculum of bacteria ($w(x,0) = 0.5$) enables the bacteria to proliferate at the wound

Poor clotting

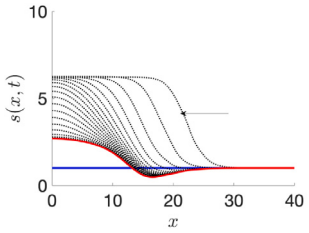

(a) Signal concentration ($s(x,t)$): $\beta_{sm} = 4$.

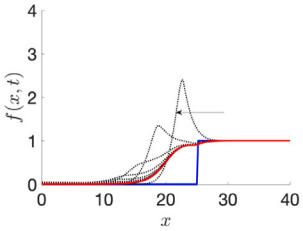

(b) Fibroblast and immune cell density ($f(x,t)$): $\beta_{sm} = 4$.

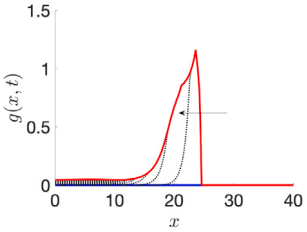

(c) Granulation tissue thickness ($g(x,t)$): $\beta_{sm} = 4$.

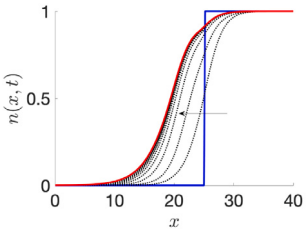

(d) Keratinocyte thickness ($n(x,t)$): $\beta_{sm} = 4$.

Cellular senescence

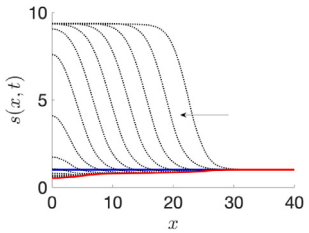

(e) Signal concentration ($s(x,t)$): $\beta_{fcs} = 1$.

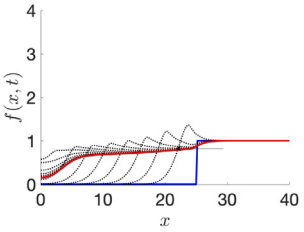

(f) Fibroblast and immune cell density ($f(x,t)$): $\beta_{fcs} = 1$.

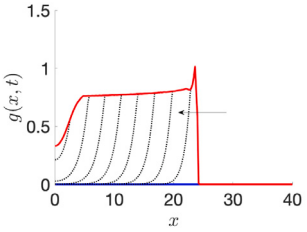

(g) Granulation tissue thickness ($g(x,t)$): $\beta_{fcs} = 1$.

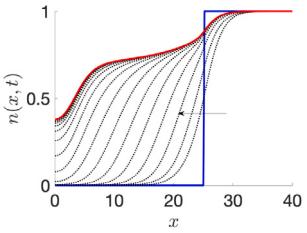

(h) Keratinocyte thickness ($n(x,t)$): $\beta_{fcs} = 1$.

Fig. 5. Numerical solutions for (1)–(8) with ICs and BCs in Table 2, for $w_0 = 0$. Solutions are shown in steps of $t = 8$ using parameters in Table 3 except for either $\beta_{sm} = 4$ or $\beta_{fcs} = 1$. Arrows indicate the direction of variable changes over time, with the blue line representing the initial condition and the red line representing the steady-state solution. (For interpretation of the references to colour in this figure legend, the reader is referred to the web version of this article.)

site, where a greater density can be observed ($w \approx 0.9$) as seen in Fig. 6(e). Higher bacterial density results in lower nutrient concentrations within the wound area (Fig. 6(f)), therefore fibroblasts and immune cells have insufficient nutrients to travel towards the wound centre (Fig. 6(g)). As a consequence, the bacteria towards the wound centre cannot be cleared and reach a non-zero steady state. Furthermore, fibroblasts/immune cells are only able to lay granulation tissue near the wound edge (Fig. 6(h)). Consequently, wound closure does not occur at the centre and is only observed for $x \in (20, 25)$.

A contaminated wound will heal successfully provided the initial inoculum is at a low level, and resembles earlier results (with no bacterial infection) of normal repair. Increase in initial bacterial density, impacts on the healing path and can delay or prevent complete wound recovery.

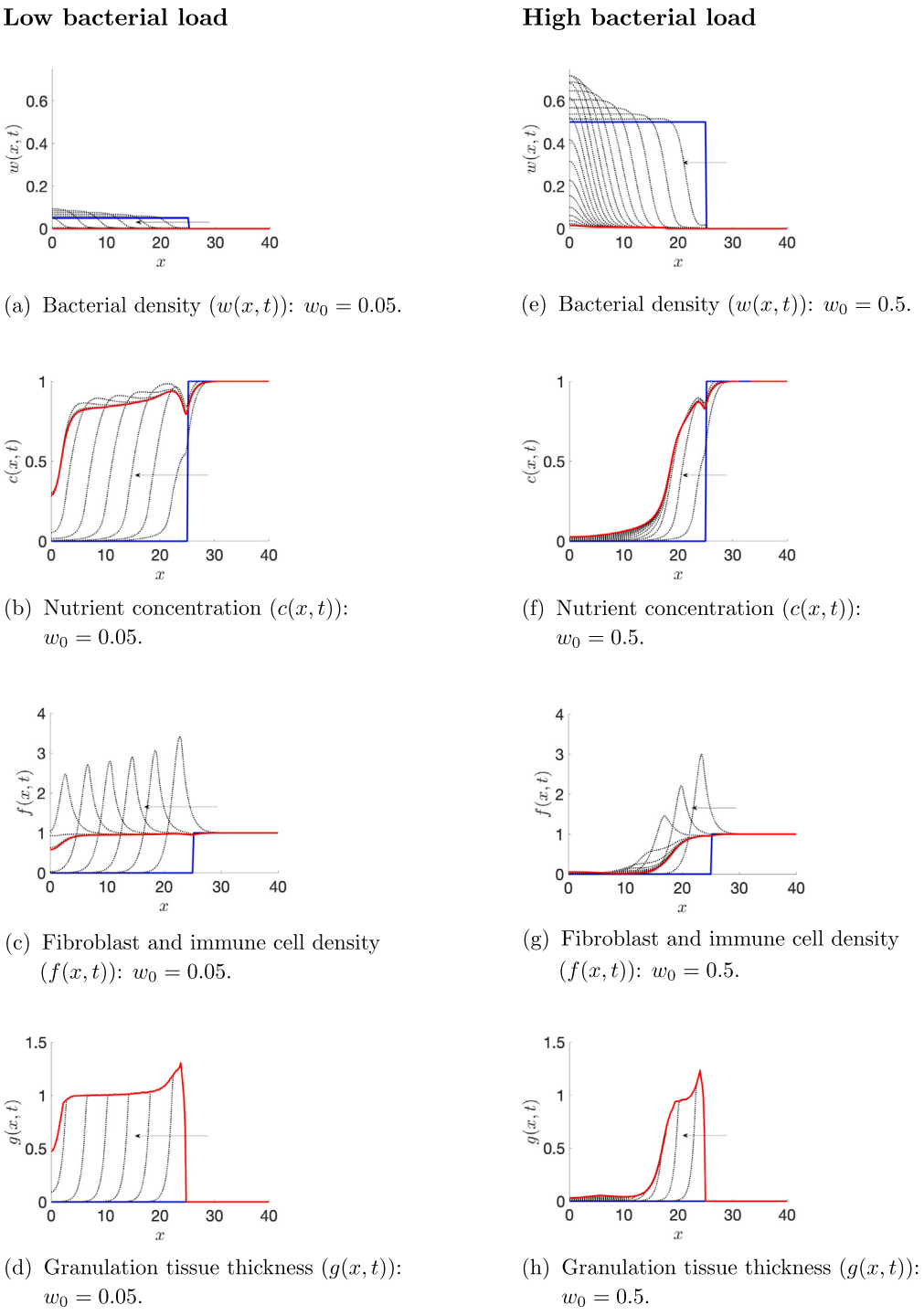

(a) Bacterial density ($w(x,t)$): $w_0 = 0.05$.

(e) Bacterial density ($w(x,t)$): $w_0 = 0.5$.

(b) Nutrient concentration ($c(x,t)$): $w_0 = 0.05$.

(f) Nutrient concentration ($c(x,t)$): $w_0 = 0.5$.

(c) Fibroblast and immune cell density ($f(x,t)$): $w_0 = 0.05$.

(g) Fibroblast and immune cell density ($f(x,t)$): $w_0 = 0.5$.

(d) Granulation tissue thickness ($g(x,t)$): $w_0 = 0.05$.

(h) Granulation tissue thickness ($g(x,t)$): $w_0 = 0.5$.

Fig. 6. Numerical solutions for (1)–(8) with ICs and BCs in Table 2, for the case of a bacterial infection, where $w_0 = 0.05$ or $w_0 = 0.5$ and $\beta_{wn} = 0.001$. Solutions are shown in time steps of $t = 8$, using parameter values from Table 3. Arrows indicate the direction of variable changes over time, with the blue line representing the initial condition and the red line representing the steady-state solution. (For interpretation of the references to colour in this figure legend, the reader is referred to the web version of this article.)

3. BG fibres as a potential treatment for chronic wounds

3.1. Methods

We extend the model of Section 2 to investigate BG fibre treatment doped with antimicrobial metal ions (e.g. silver) and wound healing ions (e.g. copper) on the chronic wounds and the wound healing process. To achieve this, we draw on the results from Section 2.2 to simulate a wound that becomes chronic due to the presence of a bacterial infection and/or impaired wound healing mechanisms, such as poor vascularisation, poor clotting, and cellular senescence.

3.1.1. Modelling assumptions

When incorporating BG fibre treatment, the model is expanded with the following assumptions:

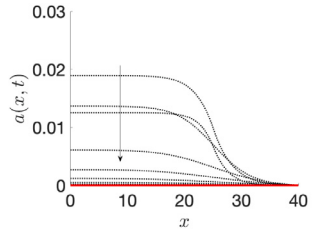

(a) Antimicrobial ion concentration ($a(x,t)$).

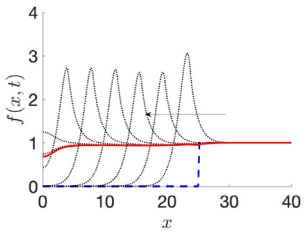

(d) Fibroblast and immune cell density ($f(x,t)$).

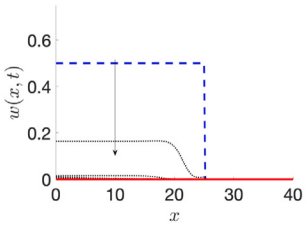

(b) Bacteria density ($w(x,t)$).

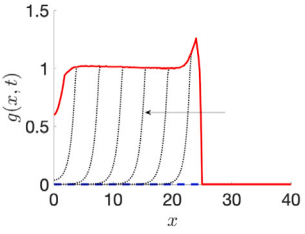

(e) Granulation tissue thickness ($g(x,t)$).

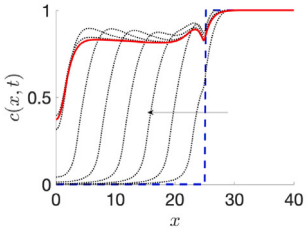

(c) Nutrient concentration ($c(x,t)$).

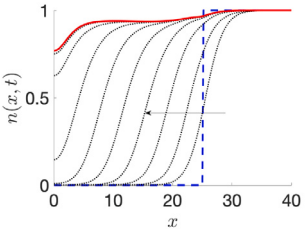

(f) Keratinocyte thickness ($n(x,t)$).

Fig. 7. Numerical solutions for (10)–(20) with ICs and BCs in Tables 2 and 6, for the case of a bacterial infection, where $w_0 = 0.5$ and $\beta_{wn} = 0.001$. Solutions are shown in time steps of $t = 8$, using parameter values from Tables 3 and 11, except for $\gamma = 0$. Arrows indicate the direction of variable changes over time, with the blue line representing the initial condition and the red line representing the steady-state solution. (For interpretation of the references to colour in this figure legend, the reader is referred to the web version of this article.)

- **Migration support**: Fibroblasts/immune cells and keratinocytes use the BG fibres ($\phi(\mathbf{x},t)$) as an additional scaffold to migrate via chemotaxis (chemotaxis terms in Eqs. (10) and (14)) (Norris et al., 2020).
- **Degradation dynamics**: BG fibres ($\phi(\mathbf{x},t)$) degrade homogeneously throughout the wound (Eq. (18)) as all the fibres are immersed in wound fluid and they degrade at a constant rate due to each fibre being ribbon shaped (Poologasundarampillai et al., 2014).
- **Ion release**: BG fibres ($\phi(\mathbf{x},t)$) release ions as they degrade, forming two distinct populations: antibacterial ions ($a(\mathbf{x},t)$) and wound-healing ions ($h(\mathbf{x},t)$) (ion release terms in Eqs. (19) and (20)).
  - **Wound-healing ions**: These are released at a constant rate from the fibre and spread via diffusion. They have the effect of enhancing the growth rate of fibroblast/immune and keratinocyte cells. The ions "decay" via sequestration by these cells and naturally in the wound environment (Eq. (19)) (Paterson et al., 2020; Zhao et al., 2015).
  - **Antimicrobial ions**: These are released at a constant rate from the fibre and spread via diffusion. They kill wound bacteria and are sequestered in the wound environment and by bacteria (Eq. (20)) (Shirgill et al., 2023; Wilkinson et al., 2018).

Table 4 summarises typical timescales for key BG fibre treatment processes from the literature, which are used to constrain model parameters. For example, biofilm formation and its eradication by BG fibres occur on shorter timescales than chronic wound healing, allowing parameters to be tuned accordingly. Likewise, BG fibres dissolve within roughly a week, compared with wound healing over about a month, helping to estimate dissolution rates and the number of applications required before healing.

3.1.2. Model formulation

Given the assumptions in Section 3.1.1, the full set of non-dimensionalised equations of the extended model incorporating BG fibre treatment (new variables listed in Table 5), are:

$$\frac{\partial n}{\partial t} = \text{RHS[Eq. (1)]} - \underbrace{\nabla\cdot\left(n\chi_n\sigma_{n\phi}H(\phi)\nabla s\right)}_{\text{Chemotaxis influenced by }\phi} + \underbrace{\frac{\beta_{nh}h}{1+s/\gamma_{ncs}}n\left(1-\frac{n}{\kappa_n}\right)}_{\text{Stimulation}}, \tag{10}$$

$$\frac{\partial m}{\partial t} = \text{RHS[Eq. (2)]}, \tag{11}$$

$$\frac{\partial d}{\partial t} = \text{RHS[Eq. (3)]}, \tag{12}$$

$$\frac{\partial g}{\partial t} = \text{RHS[Eq. (4)]} + \underbrace{\frac{\beta_{ghf}hcf}{1+w/\gamma_{gw}}H(s-\bar{s})H(\bar{c}-c)}_{\text{Production}}, \tag{13}$$

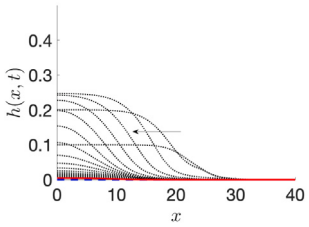

(a) Wound healing ion concentration ($h(x,t)$).

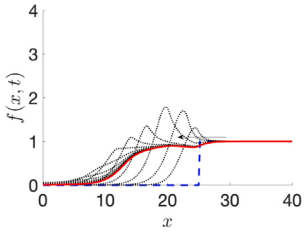

(c) Fibroblast and immune cell density ($f(x,t)$).

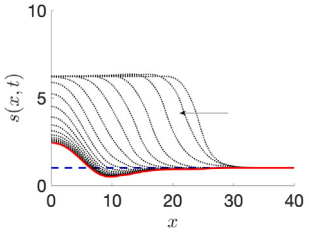

(b) Signal concentration ($s(x,t)$).

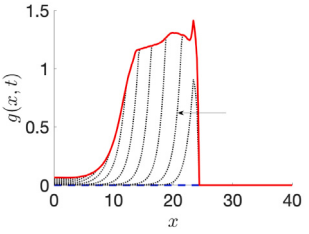

(d) Granulation tissue thickness ($g(x,t)$).

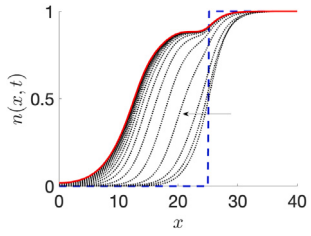

(e) Keratinocyte thickness ($n(x,t)$).

Fig. 8. Numerical solutions for (10)–(20) with ICs and BCs in Tables 2 and 6, for the case of no bacterial infection ($w_0 = 0$) and impaired wound healing mechanisms, where $\gamma_b = 0.85$, $\beta_{sm} = 4$ and $\beta_{fcs} = 1$. Solutions are shown in time steps of $t = 8$, using parameter values from Tables 3 and 11. Arrows indicate the direction of variable changes over time, with the blue line representing the initial condition and the red line representing the steady-state solution. (For interpretation of the references to colour in this figure legend, the reader is referred to the web version of this article.)

Table 4
Key events that occur in the process of chronic wound healing with BG fibres and their associated timescales.

Event	Timescale	Reference
Biofilm eradication by BG fibres	~ 1 day	Paterson et al. (2020), Jung et al. (2019)
Mature biofilm formation	~ 1-2 days	Paterson et al. (2020), Jung et al. (2019)
Complete dissolution of BG fibres in wound	~ 1 week	Poologasundarampillai et al. (2014), Norris et al. (2020)
Chronic wound heals after treatment with BG fibres	~ 1 month	Cole

Table 5
Variable definitions from the wound healing model (10)-(20).

Variables	Description
$\phi(\mathbf{x},t)$	Volume fraction of the BG fibres
$h(\mathbf{x},t)$	Wound healing ion cross sectional concentration
$a(\mathbf{x},t)$	Antibacterial ion cross sectional concentration

$$\frac{\partial f}{\partial t} = \text{RHS[Eq. (5)]} - \underbrace{\nabla\cdot\left(f\chi_f\sigma_{f\phi}H(\phi)\nabla s\right)}_{\text{Chemotaxis influenced by }\phi} + \underbrace{\beta_{fh}hf H(s-\bar{s})}_{\text{Stimulation}}, \tag{14}$$

$$\frac{\partial c}{\partial t} = \text{RHS[Eq. (6)]}, \tag{15}$$

$$\frac{\partial w}{\partial t} = \text{RHS[Eq. (7)]} - \underbrace{\delta_{wa}wa}_{\text{Clearance}}, \tag{16}$$

$$\frac{\partial s}{\partial t} = \text{RHS[Eq. (8)]} + \underbrace{\frac{\beta_{sfh}}{\beta_{sc}}fh(1+\beta_{sc}H(\bar{c}-c))}_{\text{Signal production}}, \tag{17}$$

$$\frac{\partial \phi}{\partial t} = \underbrace{-\delta_\phi H(\phi)}_{\text{Degradation}}, \tag{18}$$

$$\frac{\partial h}{\partial t} = \underbrace{\nabla\cdot\left(D_h\nabla h\right)}_{\text{Diffusion}} + \underbrace{\delta_\phi\phi_0 H(\phi)\gamma\xi}_{\text{Ion release}} - \underbrace{h(\delta_{hf}f+\delta_{hn}n+\delta_h)}_{\text{Decay and cell usage}}, \tag{19}$$

$$\frac{\partial a}{\partial t} = \underbrace{\nabla\cdot\left(D_a\nabla a\right)}_{\text{Diffusion}} + \underbrace{\delta_\phi\phi_0 H(\phi)\xi}_{\text{Ion release}} - \underbrace{a(\delta_{aw}w+\delta_a)}_{\text{Decay and cell usage}}, \tag{20}$$

where $H(.)$ is the Heaviside function, defined in Section 2.1.2 and RHS is 'Right hand side'. It is assumed that though the fibre strands do degrade they are still present as strands, so that the fibre scaffold remains

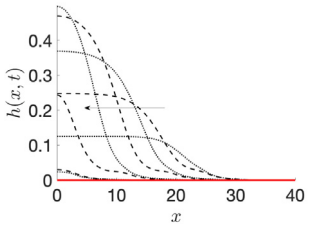

(a) Wound healing ion concentration ($h(x,t)$).

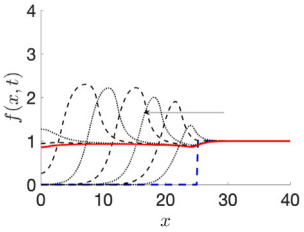

(c) Fibroblast and immune cell density ($f(x,t)$).

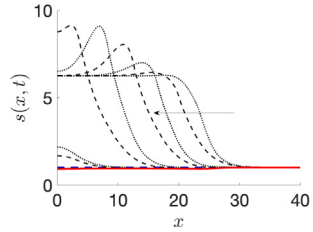

(b) Signal concentration ($s(x,t)$).

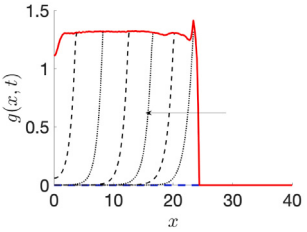

(d) Granulation tissue thickness ($g(x,t)$).

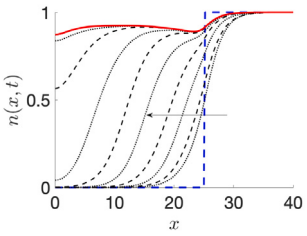

(e) Keratinocyte thickness ($n(x,t)$).

Fig. 9. Numerical solutions for (10)–(20) with ICs and BCs in Tables 2 and 6, for the case of no bacterial infection ($w_0 = 0$) and impaired wound healing mechanisms, where $\gamma_b = 0.85$, $\beta_{sm} = 4$ and $\beta_{fcs} = 1$. Solutions are shown in time steps of $t = 10$, using parameter values from Tables 3 and 11. Here BG fibres are reapplied once they are dissolved within the wound (at time points corresponding to the dashed lines). Arrows indicate the direction of variable changes over time, with the blue line representing the initial condition and the red line representing the steady-state solution. (For interpretation of the references to colour in this figure legend, the reader is referred to the web version of this article.)

mostly intact throughout the life time of the BG fibres; consequently we used $H(\phi)$ in the chemotaxis terms for n and f to reflect this.

The dimensional model along with dimensional initial conditions, boundary conditions and parameter definitions are provided in Appendix B.

3.1.3. Modelling a one-dimensional wound

We continue to model the wound in one dimension, focusing on the dynamics along the x-axis. We assume that the BG fibres are uniformly spread over the entire wound, occupying the same scaled volume fraction. We will investigate the cases with and without antimicrobial and wound-healing ion doping. Table 6 summarises the additional initial and boundary conditions used in the simulations to follow.

3.2. Results

The extended model focuses on chronic wounds and incorporates parameter values representing the chronic wound state, as identified in Section 2. Table 7 summarises the additional non-dimensional parameters used in (10)–(20); full justification is provided in Shirgill (2024). Briefly, ϕ_0 and δ_ϕ were estimated from BG fibre physical properties (Norris et al., 2020; Poologasundarampillai et al., 2014); ξ, D_h, D_a, $\sigma_{n\phi}$, $\sigma_{f\phi}$ were selected to be order-of-magnitude consistent with diffusion/chemotaxis parameters in the no-treatment model; γ, δ_{hf},

Table 6
Non-dimensional initial conditions (ICs) and boundary conditions (BCs) for treatment variables in (10)–(20). Subtable (a) lists ICs and Dirichlet BCs at $x = L$; subtable (b) lists Neumann (no-flux) BCs for derivatives at the symmetry boundary $x = 0$.

(a) Variables: ICs and BCs at $x = L$ (Dirichlet).

Variable	IC ($x \in [0, L_w]$)	IC ($x \in (L_w, L]$)	BC ($x = L$)
ϕ	1	0	–
h	0	0	0
a	0	0	0

(b) Neumann/no-flux conditions at $x = 0$.

Quantity	BC ($x = 0$)
h_x	0
a_x	0

Notes: (i) A dash "–" indicates no Dirichlet BC is imposed at $x = L$ for that variable. (ii) Homogeneous Neumann conditions at $x = 0$ enforce no-flux for the ion fields h and a.

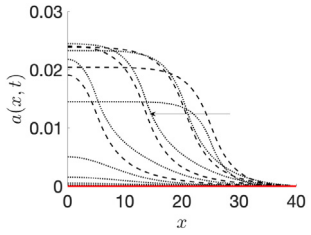

(a) Antimicrobial ion concentration ($a(x,t)$).

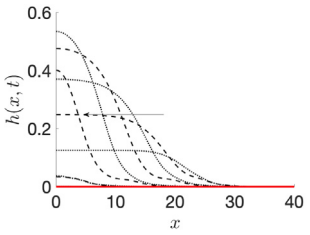

(c) Wound healing ion concentration ($h(x,t)$).

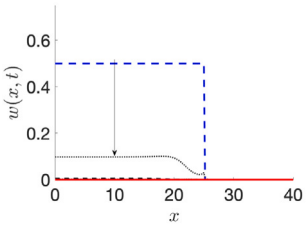

(b) Bacteria density ($w(x,t)$).

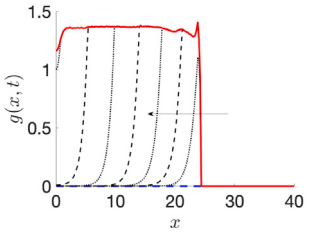

(d) Granulation tissue thickness ($g(x,t)$).

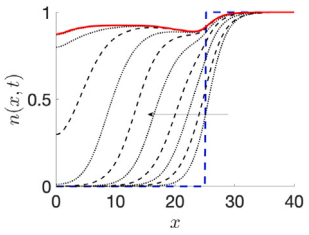

(e) Keratinocyte thickness ($n(x,t)$).

Fig. 10. Numerical solutions for (10)–(20) with ICs and BCs in Tables 2 and 6, for the case of a bacterial infection ($w_0 = 0.5$ and $\beta_{wn} = 0.001$) and impaired wound healing mechanisms, where $\gamma_b = 0.85$, $\beta_{sm} = 4$ and $\beta_{fcs} = 1$. Solutions are shown in time steps of $t = 10$, using parameter values from Tables 3 and 11. Here BG fibres are reapplied once they are dissolved within the wound (at time points corresponding to the dashed lines). Arrows indicate the direction of variable changes over time, with the blue line representing the initial condition and the red line representing the steady-state solution. (For interpretation of the references to colour in this figure legend, the reader is referred to the web version of this article.)

Table 7
Default additional non-dimensional parameter values for modelling wound treatment in the system of Eqs. (10)-(20). Where full justification for parameter values can be found in Shirgill (2024).

Parameter	Value	Parameter	Value	Parameter	Value
ϕ_0	0.05	γ	5	ξ	1
D_h	1.5	D_a	1.5	$\sigma_{n\phi}$	1
$\sigma_{f\phi}$	1	δ_ϕ	0.05	δ_{hf}	0.3
δ_{hn}	0	δ_h	0	δ_{aw}	0.1
δ_a	0.1	β_{nh}	0	δ_{wa}	20
β_{fh}	0	β_{ghf}	0	β_{sfh}	10

Table 8
Parameter values representing key traits that differentiate acute and chronic wounds. Chronic wounds are characterised by impaired wound healing mechanisms, including poor vascular perfusion (γ_b), reduced clotting efficiency (β_{sm}), cellular senescence (β_{fcs}), and higher bacterial load (w_0). These values are used to model chronic wound dynamics in the study.

Chronic wound trait	Parameter	Acute wound value	Chronic wound value
Poor vascular perfusion	γ_b	0.6	0.85
Poor clotting	β_{sm}	6	4
Cellular senescence	β_{fcs}	3	1
Bacterial infection	w_0	0.05	0.5

β_{sfh}, δ_{wa} were calibrated to reproduce qualitatively desirable behaviour (with their effects explored in subsequent sections); and remaining low-sensitivity parameters were fixed at nominal baseline values (0 for 'off', 0.1 for 'on').

Table 8 highlights the key differences in parameter values between acute and chronic wounds, where parameter values were chosen so that simulations produced qualitatively expected healing processes in either an acute or chronic setting. This framework enables an evaluation of how BG fibres can modulate these parameters to promote wound healing.

Here, we explore how BG fibre can accelerate wound healing in chronic wounds through the release of antimicrobial ions, wound healing ions, or a combination of both.

3.2.1. Antimicrobial treatment

Results in Section 2.2.3 demonstrate that bacterial infections can significantly impede wound healing, with sufficiently high bacterial

densities preventing wound closure altogether. Here, we investigate the impact of BG fibres doped with antimicrobial ions only (i.e $\gamma = 0$) on wound healing (Fig. 7), noting the untreated case is shown in the right-hand panel of Fig. 6. As these BG fibres degrade, they release antimicrobial ions that diffuse throughout the wound area and degrade over time due to natural loss or bacterial uptake (Fig. 7(a)). This release rapidly reduces bacterial density across the wound (Fig. 7(b)).

With the bacterial load lowered, nutrient consumption by the bacteria is minimised compared to the untreated case (Fig. 7(c)). This ensures adequate nutrient supply to the wound edge, supporting fibroblast and immune cell migration and proliferation (Fig. 7(d)). These cells deposit granulation tissue (Fig. 7(e)), which facilitates nutrient perfusion towards the wound centre, further promoting fibroblast and immune cell activity. This process creates a positive feedback loop of tissue deposition and nutrient delivery. Finally, the granulation tissue supports the formation of a keratinocyte layer across the wound surface (Fig. 7(f)), signifying successful wound closure and healing.

Whether the wound heals or reaches a non-healed steady state depends on the antimicrobial death rate of bacteria (δ_{wa}). When this parameter is reduced tenfold (see Fig. 11 in Appendix D), results indicate that although bacterial populations initially decline, they begin to recover and proliferate at the wound centre, stalling wound healing and resulting in a non-healed wound. These results highlight the critical role of strong antimicrobial activity in rapidly eradicating biofilms to facilitate successful wound healing.

3.2.2. Wound healing treatment

Next, we examine the effect of BG fibres releasing ions that stimulate wound healing in the absence of a bacterial infection. This scenario assumes that wound healing mechanisms are impaired through poor vasculature, poor clotting, and cellular senescence, as identified in Section 2.2.2 as key factors distinguishing acute from chronic wounds. As shown in Fig. 8(a), BG fibres degrade and release wound healing ions, which are subsequently removed through natural loss or interactions with cells, similar to the process illustrated in Fig. 7(a).

The signalling molecule concentration profile closely resembles that of an untreated poor-clotting wound (Fig. 8(b)), despite the ions stimulating some secretion of signalling molecules by fibroblasts and immune cells. While small peaks in fibroblast and immune cell density move closer to the wound centre compared to the untreated case (Fig. 8(c)), the concentration remains insufficient to support significant fibroblast/immune cell migration and proliferation. Consequently, more granulation tissue is deposited with treatment than without (Fig. 8(d)), but the wound centre remains inadequately filled. This limited granulation tissue prevents the formation of a complete keratinocyte layer (Fig. 8(e)), leaving the wound in a non-healed state.

Next, we investigate the effect of reapplying fibres after they have fully degraded. Since the fibres degrade at a linear rate, reapplication occurs every $t = 20$ (approximately every 6 days) in regions where $d(x,t) + g(x,t) < 0.8$ (which indicates regions where the wound has yet to heal). Once $d(x,t) + g(x,t) \geq 0.8$ for $0 < x < L$, no further fibres are applied. This approach results in higher wound healing ion concentrations compared to a single application (compare Figs. 9(a) and 8(a)).

The increased ion concentrations stimulate fibroblasts and immune cells to secrete greater amounts of signalling molecules, leading to higher peaks in signalling molecule concentrations throughout the wound (Figs. 9(b) and 9(c)). As fibroblasts and immune cells migrate across the entire wound domain, they deposit granulation tissue throughout the wound, enabling the formation of a complete keratinocyte layer. This process results in successful wound healing (Figs. 9(d) and 9(e)).

This reapplication strategy demonstrates that higher signalling molecule concentrations (Fig. 8(b)) can be achieved through the stimulation of fibroblast and immune cell activity at the wound edge, enhancing their ability to secrete signalling molecules (Fig. 8(c)).

3.2.3. Antimicrobial and wound healing treatment

Finally we look at the case when a wound is chronic due to impaired wound healing mechanisms, such as poor vasculature, poor clotting, cellular senescence as well as containing a bacterial infection. In this case, BG fibres are reapplied once fully dissolved and fibres release both antimicrobial and wound healing ions. It is important to note that applying antimicrobial ions alone would eradicate the bacterial infection; however, due to the underlying impaired wound healing mechanisms, the wound would remain unhealed. Therefore, the inclusion of wound healing ions is critical to stimulate the necessary cellular processes and promote tissue regeneration, ultimately enabling complete wound closure.

During treatment, the bacterial population is suppressed very early on in the stages of wound healing (Fig. 10(b)) by the antimicrobial ions released from the BG fibres (Fig. 10(a)). Fibroblasts lay down granulation tissue (Fig. 10(d)) and take up wound healing ions so that the ion concentration decreases (observing Fig. 10(c)). Once keratinocyte layer and granulation tissue reach sufficient levels in the wound centre, the wound is healed (i.e. when $n(x,t)$ and $g(x,t)$ approach 1 throughout the original wound area in Figs. 10(e) and 10(d) respectively).

It is important to note that timescales are a critical consideration for combination therapy involving both antimicrobial and wound healing ions. Antimicrobial ions must act quickly to eradicate the bacterial infection at an early stage, as the resolution of infection is a prerequisite for initiating subsequent healing processes. Without this rapid bacterial clearance, the impaired wound environment would continue to hinder fibroblast activity, granulation tissue formation, and re-epithelialisation, delaying or preventing wound closure.

Further investigation identified that one of the most important parameters involved in whether a wound heals or not is the increased secretion of signalling molecule by fibroblasts due to the presence of wound healing ions (see Fig. 12 in Appendix D). A reduction in β_{sfh} by an order of magnitude causes the wound to transition from a healed to a non-healed steady state. Specifically, reducing β_{sfh} from 10 to 1 leads to insufficient signalling molecule concentrations within the wound, preventing adequate fibroblast and immune cell proliferation Consequently, fibroblasts fail to migrate effectively or produce sufficient granulation tissue, ultimately leaving the wound unhealed. These findings underscore the pivotal role of fibroblast-driven processes in wound healing and highlight how the interplay of signalling molecules and wound healing ions determines the success or failure of healing.

4. Discussion

In this paper we used novel mathematical models to investigate the healing processes during the proliferation phase of full-thickness wounds, to highlight causes of chronicity and treatment using ion-doped BG fibres. The model incorporates the collective and interactive behaviour of fibroblasts, keratinocytes, granulation tissue, signals, nutrients, healthy and unhealthy wound area as healing persists and simulations presented here illustrate normal and abnormal healing scenarios.

In the simulations conducted, the key factors investigated included nutrient supply, signalling molecule production (either growth factors or cytokines), and cellular senescence. Next, we examined healing dynamics in the presence of bacteria at the wound site. The model predicts that bacterial burden impedes healing, with the extent of wound closure decreasing as bacterial load increases, consistent with clinical and experimental evidence on infection-related delays in healing (James et al., 2008; Bowler et al., 2001; Percival et al., 2012; Metcalf and Bowler, 2013). This indicates greater impairment in wounds with higher levels of infection. Debridement is commonly used in clinical settings to effectively reduce bacterial populations; however, it may not fully eliminate them, especially in cases involving biofilm-forming bacteria. These residual bacteria can continue to impede nutrient availability and fibroblast activity, as suggested by our results. This highlights

the need for adjunctive treatments, such as antimicrobial therapies or biomaterials like bioactive glass fibres, to complement debridement by targeting remaining bacterial populations and supporting the wound healing process.

This granulation-centric model differs from classical proliferative-phase models as they typically emphasise either explicit angiogenesis via capillary tip migration and sprout branching (Pettet et al., 1996; Olsen et al., 1997; Machado et al., 2011; Vermolen and Javierre, 2012; Valero et al., 2013) or explicit fibroblast/collagen interactions (Olsen et al., 1998; Dallon and Sherratt, 1998; Dallon et al., 1999, 2001; McDougall et al., 2006; Haugh, 2006). In contrast, in our model, we track the production of granulation tissue as the organising variable for progress through proliferation, with angiogenesis and fibroblast/collagen activity represented implicitly via support to perfusion/nutrient delivery and fibroblast-driven matrix deposition. This allows us to couple factors of chronicity (impaired perfusion/vascular support, clotting deficits, cellular senescence, bacterial burden) and treatment via ion-doped BG fibres (consisting of antimicrobial and wound healing ion populations). As a result we can study therapy sequencing and timescales easier than these traditional proliferative-phase models.

Our simulations are consistent with qualitative dependencies reported in angiogenesis-centric studies: reduced vascular support impairs nutrient availability and slows fibroblast proliferation and re-epithelialisation (Pettet et al., 1996; Machado et al., 2011). Likewise, results where reduced signalling or fibroblast activity limits closure align with fibroblast/collagen frameworks emphasising that adequate fibroblast motility, secretion and matrix deposition are necessary for timely healing (McDougall et al., 2006; Haugh, 2006; Menon et al., 2012).

This study explored the potential of BG fibres to aid in chronic wound healing through the release of antimicrobial and wound healing ions. Results indicate that antimicrobial ions effectively reduce bacterial populations, thereby minimising nutrient competition and facilitating fibroblast and immune cell activity, granulation tissue formation, and eventual wound closure. However, the antimicrobial death rate (δ_{wa}) plays a crucial role; inadequate bacterial clearance can result in non-healed steady states.

The release of wound healing ions enhances fibroblast and immune cell activity by stimulating signalling molecule secretion and promoting granulation tissue deposition. Reapplying BG fibres after their degradation further boosts ion concentrations, leading to increased signalling molecule levels and improved granulation tissue coverage, thereby supporting wound healing under suitable conditions.

In more complex wound scenarios involving poor vasculature, clotting deficiencies, cellular senescence, and bacterial infections, the combination of antimicrobial and wound healing ions improves outcomes. However, the timing of their action is critical; antimicrobial ions must act rapidly to eliminate bacterial populations early in the healing process, creating a conducive environment for wound healing ions to support fibroblast activity, granulation tissue formation, and re-epithelialisation. However, reduced fibroblast stimulation or insufficient signalling molecule secretion, such as from lower secretion rates (β_{sfh}) may limit healing, highlighting the importance of these parameters.

These findings underscore the complex interplay of biological and environmental factors in wound healing and highlight the critical importance of effective infection control and targeted treatments in chronic wounds. Future work should aim to expand its scope. For instance,

- Expanding the model to simulate different chronic wound etiologies, such as venous leg ulcers, pressure ulcers, and diabetic foot ulcers, could offer tailored insights into treatment strategies.
- Including variability in patient conditions, such as age, comorbidities (e.g. diabetes), and differences in immune response, would enhance the model's clinical relevance and predictive power.
- Future work should incorporate a more complex representation of bacterial dynamics, such as including multiple bacterial species with distinct behaviours, which could provide a deeper understanding of the challenges posed by polymicrobial infections and microbial resistance.

By addressing these directions, the model can evolve into a robust tool for exploring wound healing dynamics across various contexts, aiding both research and clinical decision-making. This continued development will further enhance our understanding of chronic wound pathology and the optimisation of innovative treatments like BG fibres.

5. Conclusion

In summary, our model provides a framework for the proliferative phase that captures how perfusion, signalling, senescence, and bacterial burden jointly govern wound closure. Simulations reproduce known qualitative dependencies and highlight infection control critical for successful wound healing. Ion-doped bioactive glass fibres can shift non-healing trajectories towards closure when antimicrobial action rapidly reduces bacterial load and when wound healing ions sustain fibroblast activity and signalling; insufficient clearance or weak stimulation leads to stalled healing. By enabling exploration of therapy sequencing, dosing, and timing, the model provides actionable hypotheses for optimising BG-based interventions.

CRediT authorship contribution statement

Sandeep Shirgill: Writing – original draft, Methodology, Investigation, Formal analysis. **Najida Begum:** Writing – original draft, Conceptualization. **Sarah A. Kuehne:** Supervision, Project administration, Funding acquisition, Conceptualization. **Gowsihan Poologasundarampillai:** Supervision. **Sara Jabbari:** Writing – review & editing, Supervision, Conceptualization. **John Ward:** Writing – review & editing, Supervision, Conceptualization.

Acknowledgements

Support from the Biotechnology and Biological Sciences Research Council, United Kingdom (www.ukri.org/councils/bbsrc/) is greatly acknowledged. We would also like to acknowledge support from the Engineering and Physical Sciences Research Council, United Kingdom (grant code: EP/V051342/1,www.ukri.org/councils/epsrc/) The funders had no role in study design, data collection and analysis, decision to publish, or preparation of the manuscript. SJ thanks the Leverhulme Trust (RPG-2019-382). Code is available at: Shirgill, S. (2025) *Numerical solutions for chronic wound healing with treatment PDEs.* University of Birmingham.
10.25500/edata.bham.00001238.

Declaration of competing interest

The authors declare the following financial interests/personal relationships which may be considered as potential competing interests: Sandeep Shirgill reports financial support was provided by Biotechnology and Biological Sciences Research Council. If there are other authors, they declare that they have no known competing financial interests or personal relationships that could have appeared to influence the work reported in this paper.

Table 9
Parameter definitions and units from the wound healing model (21)-(28).

Parameters	Description	Units
D_n	Diffusion coefficient of n	mm^2 h^{-1}
χ_n	Chemotaxis coefficient of n	mm^3 (gh)$^{-1}$
σ_n	Chemotaxis ratio of n for g	Dimensionless
β_n	n birth rate	mm^2 (gh)$^{-1}$
γ_{ncs}	n cell birth constant	g mm^{-2}
κ_n	n maximum capacity	mm
γ_{nc}	n inhibited by nutrient availability	g mm^{-2}
δ_{nc}	n cell death rate from lack of c	h^{-1}
δ_{mf}	m removed by f	mm^2 (cells h)$^{-1}$
δ_{ms}	Enhanced removal constant of m due to s	mm^4 (g h cells)$^{-1}$
δ_m	Natural death rate of m	h^{-1}
β_{gsf}	Enhanced g production due to lack of s	mm^5 g^{-2} (cells h)$^{-1}$
δ_{gc}	g loss rate due to lack of c	mm^3 (gh)$^{-1}$
β_{gf}	g production rate by f	mm^7 g^{-2} (cells h)$^{-1}$
$\bar{s}$	Critical s	g mm^{-2}
$\bar{c}$	Critical c	g mm^{-2}
D_f	Diffusion coefficient of f	mm^2 h^{-1}
χ_f	Chemotaxis coefficient of f	mm^3 (gh)$^{-1}$
σ_f	Chemotaxis ratio of f for g	Dimensionless
β_{fb}	f infiltration rate from vasculature	cells mm^{-2} h^{-1}
ρ_b	Vascular nutrient source constant	Dimensionless
γ_b	Critical vascular nutrient source constant	mm
η	Nutrient source function exponent	Dimensionless
β_{fc}	f birth rate	mm^2 (gh)$^{-1}$
κ_f	f threshold	cells mm^{-2}
β_{fcs}	Enhanced f birth rate due to s	mm^2 (gh)$^{-1}$
γ_{fcs}	f production rate by s	cells mm^{-2}
δ_{fc}	f death rate	h^{-1}
ρ_f	f death rate constant	Dimensionless
D_c	Diffusion coefficient of c	mm^2 h^{-1}
β_{cb}	c source rate from vasculature	g mm^2 h^{-1}
δ_{cn}	c consumption rate by n	mm^{-1} h^{-1}
δ_{cf}	c consumption rate by f	mm^2 (cells h)$^{-1}$
D_s	Diffusion coefficient of s	mm^2 h^{-1}
β_{sn}	s production rate by n	g mm^{-2} h^{-1}
β_{ssn}	Further s secretion rate by n	(mm h)$^{-1}$
β_{sf}	s produced by f	g (cell h)$^{-1}$
β_{ssf}	Further s secretion by f	mm^2 (cells h)$^{-1}$
β_{sc}	s production rate due to lack of c	Dimensionless
β_{sm}	s release rate from m	g mm^{-2} h^{-1}
δ_s	Decay rate of s	h^{-1}
δ_{sn}	s consumption rate by n	(mm h)$^{-1}$
δ_{sf}	s consumption rate by f	mm^2 (cells h)$^{-1}$
γ_{gf}	g inhibited by nutrient availability	g mm^{-2}

Appendix A. Dimensional equations - no treatment

The model is formulated using the assumptions outlined in Section 2. Here, n, m, d and g are thicknesses (units mm), such that the healthy skin is of thickness $d_0 + n_0$ and in the initial wound state $n = 0, d < d_0, m > 0$ and $g = 0$. The variables for f and w are cross-sectional densities, taken to be the mean density from base to the top of the wound region at coordinate $\mathbf{x}$ (units cells/mm^2). Likewise, c and s are the cross-sectional concentrations of nutrients and signal molecule (units g/mm^2). The equations for the untreated case are (21)–(28).

The Heaviside functions, $H(.)$, in the model ensures that there is significant contrast between healthy and wound scenarios. The healthy state constants for the variables, $(n, d, f, c, s) = (n_0, d_0, f_0, c_0, s_0)$, can be determined from system of non-linear algebraic equations resulting from their substitution into the equations with all of the $H(.)$ terms equalling zero. In the absence of bacteria, species n and f grow logistically at a rate enhanced by nutrients, but in the former inhibited by signalling molecule (where studies have shown that TGF-β inhibits keratinocyte production (Liarte et al., 2020)), whilst nutrients inhibit natural death of both (as cells are die at a faster rate in nutrient-deficient environments (Cui et al., 2017)). Immune cells can migrate in from the bloodstream (at a rate $\beta_{fb}k_b(d,g)$) and activated f, i.e. when $s > \bar{s}$, replicate at a faster rate. Both species migrate via diffusion and chemotaxis, the latter requiring d and g to provide a scaffold to move through. Dead material, m, decays and is removed by f to be replaced by g, however, bacteria damaged of n, d, g produces more m. The original dermal tissue that remains after injury remain static, except for bacterial damage. Granular tissue, g, is produced by activated f requiring nutrients and inhibited by bacteria; the presence of nutrients is assumed to inhibit the natural removal of g during the proliferation phase, whilst bacteria and destroy g. Nutrients are sourced via the blood stream in d and g tissue (see Section 2.1.2) and consumed by all living cells. Signalling molecules is produced by n and f at a rate enhanced by s and in low nutrient conditions $c < \bar{c}$, from dead material (such as eschar) and by immune cells in response to bacteria. These molecules decay naturally and consumed by n and f, such that a wound will be in a healed state when $s < \bar{s}$, reflecting adequate nutrients and removal of infection. Tables 9 and 10 list a description of all of the parameters, giving their representative units.

The model is non-dimensionalised using the formula listed in Appendix C, where, in particular, the variables $(n, d, f, c, s) = (n_0, d_0, f_0, c_0, s_0)$ are scaled to unity in the healthy case.

$$\begin{aligned}\frac{\partial n}{\partial t} &= \underbrace{\nabla\cdot\left(D_n\nabla n\right)}_{\text{Diffusion}} - \underbrace{\nabla\cdot\left(n\chi_n(d+\sigma_n g)\nabla s\right)}_{\text{Chemotaxis}} \\ &+ \underbrace{\frac{\beta_n c}{1+s/\gamma_{ncs}} n\left(1-\frac{n}{\kappa_n}\right)}_{\text{Birth}} - \underbrace{n\left(\frac{\delta_{nc}}{1+c/\gamma_{nc}}+\alpha_{nmw}w\right)}_{\text{Death}},\end{aligned} \tag{21}$$

$$\frac{\partial m}{\partial t} = \underbrace{w(\beta_{mn}n+\beta_{mg}g+\beta_{md}d)}_{\text{Production}} - \underbrace{mf(\delta_{mf}+\delta_{ms}s)}_{\text{Degradation}} - \underbrace{\delta_m m}_{\text{Natural loss}}, \tag{22}$$

$$\frac{\partial d}{\partial t} = \underbrace{-\alpha_{dmw}wd}_{\text{Degradation}}, \tag{23}$$

$$\frac{\partial g}{\partial t} = \underbrace{\frac{cf(\beta_{gf}+\beta_{gs}s)}{1+w/\gamma_{gw}}H(s-\bar{s})H(\bar{c}-c)}_{\text{Production}} - \underbrace{g\left(\frac{\delta_{gc}}{1+c/\gamma_{gf}}+\alpha_{gmw}w\right)}_{\text{Degradation}}, \tag{24}$$

$$\begin{aligned}\frac{\partial f}{\partial t} &= \underbrace{\nabla\cdot\left(D_f\nabla f\right)}_{\text{Diffusion}} - \underbrace{\nabla\cdot\left(f\chi_f(d+\sigma_f g)\nabla s\right)}_{\text{Chemotaxis}} + \underbrace{\beta_{fb}k_b(d,g)}_{\text{Vasculature function}} \\ &+ \underbrace{f\left(\beta_{fc}c\left(1-\frac{f}{\kappa_f}\right)+\beta_{fcs}cH(s-\bar{s})\right)}_{\text{Growth}} \\ &- \underbrace{f\left(\frac{\delta_{fc}}{1+(c+\rho_f s)/\gamma_{fcs}}+\alpha_{fmw}w\right)}_{\text{Death}},\end{aligned} \tag{25}$$

$$\frac{\partial c}{\partial t} = \underbrace{\nabla\cdot\left(D_c\nabla f\right)}_{\text{Diffusion}} + \underbrace{\beta_{cb}k_b(d,g)}_{\text{Vasculature function}} - \underbrace{c(\delta_{cn}n+\delta_{cf}f+\alpha_{cmw}w)}_{\text{Consumption}}, \tag{26}$$

$$\frac{\partial w}{\partial t} = \underbrace{w(\beta_{wc}c+\beta_{wm}m)}_{\text{Growth}} + \underbrace{\beta_{wn}H(\bar{n}-n)}_{\text{Seeding}} - \underbrace{w(\delta_w+\delta_{wf}f)}_{\text{Death}}, \tag{27}$$

$$\begin{aligned}\frac{\partial s}{\partial t} &= \underbrace{\nabla\cdot\left(D_s\nabla s\right)}_{\text{Diffusion}} \\ &+ \underbrace{\left(n(\beta_{sn}+\beta_{ssn}s)+f(\beta_{sf}+\beta_{ssf}s)\right)(1+\beta_{sc}H(\bar{c}-c))}_{\text{Production by keratinocytes and fibroblasts}} \\ &+ \underbrace{\beta_{sm}m+\beta_{sw}fw}_{\text{Additional production}} - \underbrace{s(\delta_s+\delta_{sn}n+\delta_{sf}f)}_{\text{Decay and cell usage}},\end{aligned} \tag{28}$$

Table 10
Bacteria-associated parameter definitions and units from the wound healing model (21)-(28).

Parameters	Description	Units
α_{nmw}	Death rate of n by w	mm^2 (cells h)$^{-1}$
α_{gmw}	Death rate of g by w	mm^2 (cells h)$^{-1}$
α_{dmw}	Death rate of d by w	mm^2 (cells h)$^{-1}$
α_{fmw}	Death rate of f by w	mm^2 (cells h)$^{-1}$
α_{cmw}	c consumption by w	mm^2 (cells h)$^{-1}$
γ_{gw}	g inhibited by the presence of w	cells mm^{-2}
β_{wc}	w production rate due to c	mm^2 (gh)$^{-1}$
β_{wm}	Enhanced w production rate due to m	(mm h)$^{-1}$
β_{wn}	w seeding rate from environment	cells (mm^2 h)$^{-1}$
$\bar{n}$	Critical n level	mm
δ_w	Natural loss of w	h^{-1}
δ_{wf}	Removal rate of w by f	mm^2 (cells h)$^{-1}$
β_{sw}	s production in response to w	g mm^2 (cells^2 h)$^{-1}$

Appendix B. Dimensional equations - treatment

The BG fibre is modelled as a volume fraction $\phi(\mathbf{x},t) < 1$ in the wound, whilst the ionic species ($a(\mathbf{x},t), h(\mathbf{x},t)$) are cross-sectional concentrations (with units g/mm^2). Incorporating the assumptions outlined in Section 3.1.1, then the extended wound model becomes,

$$\frac{\partial n}{\partial t} = \text{RHS[Eq. (1)]} - \underbrace{\nabla\cdot\left(n\chi_n\sigma_{n\phi}H(\phi)\nabla s\right)}_{\text{Chemotaxis influenced by }\phi} + \underbrace{\frac{\beta_{nh}h}{1+s/\gamma_{ncs}}n\left(1-\frac{n}{\kappa_n}\right)}_{\text{Stimulation}}, \tag{29}$$

$$\frac{\partial m}{\partial t} = \text{RHS[Eq. (2)]}, \tag{30}$$

$$\frac{\partial d}{\partial t} = \text{RHS[Eq. (3)]}, \tag{31}$$

$$\frac{\partial g}{\partial t} = \text{RHS[Eq. (4)]} + \underbrace{\frac{\beta_{ghf}hcf}{1+w/\gamma_{gw}}H(s-\bar{s})H(\bar{c}-c)}_{\text{Production}}, \tag{32}$$

$$\frac{\partial f}{\partial t} = \text{RHS[Eq. (5)]} - \underbrace{\nabla\cdot\left(f\chi_f\sigma_{f\phi}H(\phi)\nabla s\right)}_{\text{Chemotaxis influenced by }\phi} + \underbrace{\beta_{fh}hfH(s-\bar{s})}_{\text{Stimulation}}, \tag{33}$$

$$\frac{\partial c}{\partial t} = \text{RHS[Eq. (6)]}, \tag{34}$$

$$\frac{\partial w}{\partial t} = \text{RHS[Eq. (7)]} - \underbrace{\delta_{wa}wa}_{\text{Clearance}}, \tag{35}$$

$$\frac{\partial s}{\partial t} = \text{RHS[Eq. (8)]} + \underbrace{\frac{\beta_{sfh}}{\beta_{sc}}fh(1+\beta_{sc}H(\bar{c}-c))}_{\text{Signal production}}, \tag{36}$$

$$\frac{\partial \phi}{\partial t} = \underbrace{-\delta_\phi H(\phi)}_{\text{Degradation}}, \tag{37}$$

$$\frac{\partial h}{\partial t} = \underbrace{\nabla\cdot\left(D_h\nabla h\right)}_{\text{Diffusion}} + \underbrace{\delta_\phi\phi_0H(\phi)u_f\frac{H_d}{H}}_{\text{Ion release}} - \underbrace{h(\delta_{hf}f+\delta_{hn}n+\delta_h)}_{\text{Decay and cell usage}}, \tag{38}$$

$$\frac{\partial a}{\partial t} = \underbrace{\nabla\cdot\left(D_a\nabla a\right)}_{\text{Diffusion}} + \underbrace{\delta_\phi\phi_0H(\phi)v_f\frac{H_d}{H}}_{\text{Ion release}} - \underbrace{a(\delta_{aw}w+\delta_a)}_{\text{Decay and cell usage}}, \tag{39}$$

Table 11 list a description of all additional parameters associated with BG fibre treatment, giving their representative units. In the simulations we assume at the start of the treatment, the BG fibre is uniformly distributed across the wound at volume fraction $\phi_{max} \in (0,1)$, with an antimicrobial and wound-healing promoter ion load of a_0 and h_0, respectively.

Appendix C. Dimensionless ratios

We scale time with maximum growth rate of keratinocytes, $t \sim 1/c_0\beta_n$, and with the diffusion distance of keratinocytes over this timescale, $|\mathbf{x}| \sim \sqrt{D_n/c_0\beta_n}$. The value for c_0 was estimated from literature (5.4×10^{-8} g mm^{-2} (Schugart et al., 2008)) while β_n and D_n were tuned (2.68×10^6 mm^2 gh^{-1} and 5.78×10^{-2} mm^2 h^{-1} respectively) to align with the typical timescale for acute wound healing (2–4 weeks) and the size of typical wounds, such as diabetic foot ulcers (~5.5 cm^2 (Macioch et al., 2017)). Of particular note, the variables (n,d,f,c,s) are scaled with the healthy steady-state levels (n_0,d_0,f_0,c_0,s_0), m with d_0 and the antimicrobial a and healing h agents with the maximum antimicrobial BG fibre load (v_f)(see the equation in Box I).

Appendix D. Additional figures

See Figs. 11 and 12.

Table 11
BG fibre-associated parameter definitions and units from the wound healing model (29)-(39).

Parameters	Description	Units
ϕ_0	Initial volume fraction of BG fibres	Dimensionless
u_f	Concentration of wound healing ions within fibres	g mm^{-2}
v_f	Concentration of antibacterial ions within fibres	g mm^{-2}
D_h	Diffusion coefficient of h	mm^2 h^{-1}
D_a	Diffusion coefficient of a	mm^2 h^{-1}
$\sigma_{n\phi}$	Chemotaxis ratio of n for ϕ	Dimensionless
$\sigma_{f\phi}$	Chemotaxis ratio of f for ϕ	Dimensionless
δ_ϕ	Dissolution rate of BG fibres	h^{-1}
δ_{hf}	Uptake of wound healing ions by f	mm^2 (cells h)$^{-1}$
δ_{hn}	Uptake of wound healing ions by n	(mm h)$^{-1}$
δ_h	Natural loss of h	h^{-1}
δ_{aw}	Uptake of as by w	mm^2 (cells h)$^{-1}$
δ_a	Natural loss of a	h^{-1}
β_{nh}	n proliferation rate due to presence of h	mm^2 (g h)$^{-1}$
β_{ghf}	Enhanced production of g by f due to promotion of angiogenesis by h	mm^7 g^{-2} (cells h)$^{-1}$
β_{fh}	Enhanced f rate due to the presence of h	mm^2 (g h)$^{-1}$
β_{sfh}	Enhanced secretion of s by f due to the presence of h	mm^2 (cells h)$^{-1}$
δ_{wa}	Death of w by a	mm^2 (g h)$^{-1}$

$$\{\hat{\mathbf{x}}, \hat{t}\} = \left\{ \frac{\mathbf{x}}{\sqrt{\frac{D_n}{c_0\beta_n}}}, tc_0\beta_n \right\}$$

$$\{\hat{n}, \hat{m}, \hat{d}, \hat{g}, \hat{f}, \hat{c}, \hat{w}, \hat{s}, \hat{\phi}, \hat{h}, \hat{a}\} = \left\{ \frac{n}{n_0}, \frac{m}{d_0}, \frac{d}{d_0}, \frac{g}{d_0}, \frac{f}{f_0}, \frac{c}{c_0}, \frac{\alpha_{nmw} w}{\beta_n c_0}, \frac{s}{s_0}, \frac{\phi}{\phi_0}, \frac{h}{v_f}, \frac{a}{v_f} \right\}$$

$$\{\hat{D}_f, \hat{D}_c, \hat{D}_s, \hat{D}_h, \hat{D}_a\} = \frac{1}{D_n}\{D_f, D_c, D_s, D_h, D_a\}$$

$$\{\hat{\chi}_n, \hat{\chi}_f\} = \frac{s_0 d_0}{D_n}\{\chi_n, \chi_f\}$$

$$\{\hat{\kappa}_n, \hat{\kappa}_f\} = \left\{ \frac{\kappa_n}{n_0}, \frac{\kappa_f}{f_0} \right\}$$

$$\{\hat{\gamma}_{ncs}, \hat{\gamma}_{nc}, \hat{\gamma}_{gf}, \hat{\gamma}_{fcs}, \hat{\gamma}_b, \hat{\gamma}_{gw}\} = \left\{ \frac{\gamma_{ncs}}{s_0}, \frac{\gamma_{nc}}{c_0}, \frac{\gamma_{gf}}{c_0}, \frac{\gamma_{fcs}}{c_0}, \frac{\gamma_b}{d_0}, \frac{\gamma_{gw}\alpha_{nmw}}{\beta_n c_0} \right\}$$

$$\{\hat{\delta}_{nc}, \hat{\delta}_{mf}, \hat{\delta}_{ms}, \hat{\delta}_m, \hat{\delta}_{gc}, \hat{\delta}_{fc}, \hat{\delta}_{cn}, \hat{\delta}_{cf}, \hat{\delta}_s\} = \frac{1}{c_0\beta_n}\{\delta_{nc}, \delta_{mf} f_0, \delta_{ms} f_0 s_0, \delta_m, \delta_{gc}, \delta_{fc}, \delta_{cn} n_0, \delta_{cf} f_0, \delta_s\}$$

$$\{\hat{\delta}_{sn}, \hat{\delta}_{sf}, \hat{\delta}_w, \hat{\delta}_{wf}\} = \frac{1}{c_0\beta_n}\{\delta_{sn} n_0, \delta_{sf} f_0, \delta_w, \delta_{wf} f_0\}$$

$$\{\hat{\beta}_{gf}, \hat{\beta}_{gs}, \hat{\beta}_{fb}, \hat{\beta}_{fc}, \hat{\beta}_{fcs}, \hat{\beta}_{cb}\} = \frac{1}{\beta_n}\left\{ \frac{\beta_{gf} f_0}{d_0}, \frac{\beta_{gs} f_0 s_0}{d_0}, \frac{\beta_{fb}}{c_0 f_0}, \beta_{fc}, \beta_{fcs}, \frac{\beta_{cb}}{c_0^2} \right\}$$

$$\{\hat{\beta}_{sn}, \hat{\beta}_{ssn}, \hat{\beta}_{sf}, \hat{\beta}_{ssf}, \hat{\beta}_{sc}, \hat{\beta}_{sm}\} = \frac{1}{c_0\beta_n}\left\{ \frac{\beta_{sn} n_0}{s_0}, \beta_{ssn} n_0, \frac{\beta_{sf} f_0}{s_0}, \beta_{ssf} f_0, \beta_{sc} c_0\beta_n, \frac{\beta_{sm}\theta_p d_0}{s_0} \right\}$$

$$\{\hat{\beta}_{wn}, \hat{\beta}_{wc}, \hat{\beta}_{wm}\} = \frac{1}{c_0\beta_n}\left\{ \frac{\beta_{wn}\alpha_{nmw}}{c_0\beta_n}, \beta_{wc} c_0, \beta_{wm} d_0 \right\}$$

$$\{\hat{\beta}_{sw}, \hat{\beta}_{mn}, \hat{\beta}_{mg}, \hat{\beta}_{md}\} = \frac{1}{\alpha_{nmw}}\left\{ \frac{\beta_{sw} f_0}{s_0}, \frac{\beta_{mn} n_0}{d_0}, \frac{\beta_{mg} g_0}{d_0}, \beta_{md} \right\}$$

$$\{\hat{\alpha}_{gmw}, \hat{\alpha}_{dmw}, \hat{\alpha}_{fmw}, \hat{\alpha}_{cmw}\} = \frac{1}{\alpha_{nmw}}\{\alpha_{gmw}, \alpha_{dmw}, \alpha_{fmw}, \alpha_{cmw}\}$$

$$\{\hat{\xi}, \hat{\gamma}, \hat{\rho}_f\} = \left\{ \frac{H_d}{H}, \frac{u_f}{v_f}, \frac{\rho_f s_0}{c_0} \right\}$$

$$\{\hat{\beta}_{nh}, \hat{\beta}_{ghf}, \hat{\beta}_{fh}, \hat{\beta}_{sfh}\} = \left\{ \frac{\beta_{nh} v_f}{\beta_n c_0}, \frac{\beta_{ghf} v_f f_0}{d_0\beta_n}, \frac{\beta_{fh} v_f}{\beta_n c_0}, \frac{\beta_{sfh} f_0 v_f}{\beta_n c_0 s_0} \right\}$$

$$\{\hat{\delta}_\phi, \hat{\delta}_{hf}, \hat{\delta}_{hn}, \hat{\delta}_h, \hat{\delta}_{aw}, \hat{\delta}_a, \hat{\delta}_{wa}\} = \frac{1}{c_0\beta_n}\{\delta_\phi, \delta_{hf} f_0, \delta_{hn} n_0, \delta_h, \delta_{aw} w_0, \delta_a, \delta_{wa} v_f\}$$

Box I.

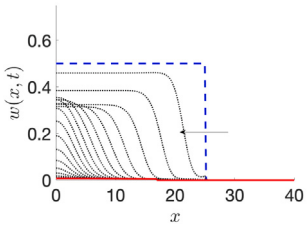

(a) Bacteria density ($w(x,t)$).

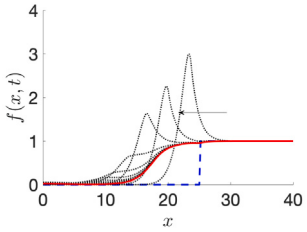

(c) Fibroblast and immune cell density ($f(x,t)$).

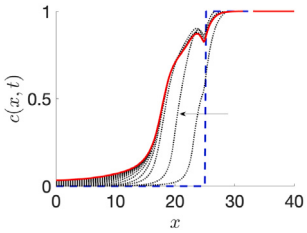

(b) Nutrient concentration ($c(x,t)$).

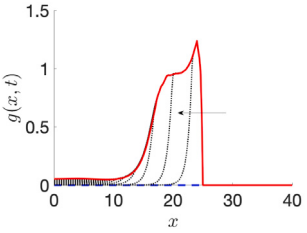

(d) Granulation tissue thickness ($g(x,t)$).

Fig. 11. Numerical solutions for (10)–(20) with ICs and BCs in Tables 2 and 6, for the case of a bacterial infection, where $w_0 = 0.5$. Solutions are shown in time steps of $t = 8$, using parameter values from Tables 3 and 11, except for $\delta_{wa} = 2$ and $\gamma = 0$. Arrows indicate the direction of variable changes over time, with the blue line representing the initial condition and the red line representing the steady-state solution. (For interpretation of the references to colour in this figure legend, the reader is referred to the web version of this article.)

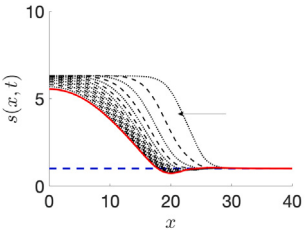

(a) Signal concentration ($s(x,t)$).

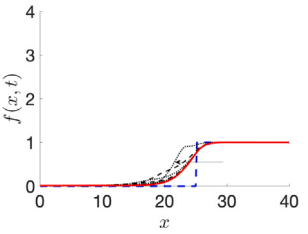

(b) Fibroblast and immune cell density ($f(x,t)$).

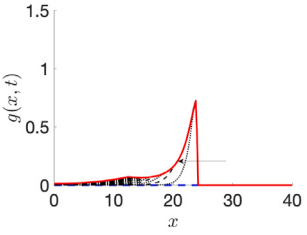

(c) Granulation tissue thickness ($g(x,t)$).

Fig. 12. Numerical solutions for (10)–(20) with ICs and BCs in Tables 2 and 6, for the case of a bacterial infection ($w_0 = 0.5$ and $\beta_{wn} = 0.001$) and impaired wound healing mechanisms, where $\gamma_b = 0.85$, $\beta_{sm} = 4$ and $\beta_{fcs} = 1$. Solutions are shown in time steps of $t = 10$, using parameter values from Tables 3 and 11, except for $\beta_{sfh} = 1$. Here BG fibres are reapplied once they are dissolved within the wound (at time points corresponding to the dashed lines). Arrows indicate the direction of variable changes over time, with the blue line representing the initial condition and the red line representing the steady-state solution. (For interpretation of the references to colour in this figure legend, the reader is referred to the web version of this article.)

References

Alhajj, M., Goyal, A., 2020. Physiology, granulation tissue. StatPearls [Internet].

Arango Duque, G., Descoteaux, A., 2014. Macrophage cytokines: involvement in immunity and infectious diseases. Front. Immunol. 5, 491.

Barrientos, S., Stojadinovic, O., Golinko, M.S., Brem, H., Tomic-Canic, M., 2008. Growth factors and cytokines in wound healing. Wound Repair Regen. 16 (5), 585–601.

Begum, N., 2009. Mathematical Modelling of Dermatological Disease and Recovery. A Doctoral Thesis.

Bowler, P.G., Duerden, B.I., Armstrong, D.G., 2001. Wound microbiology and associated approaches to wound management. Clin. Microbiol. Rev. 14 (2), 244–269.

Cai, A.Q., Landman, K.A., Hughes, B.D., 2007. Multi-scale modeling of a wound-healing cell migration assay. J. Theoret. Biol. 245 (3), 576–594.

Canadian Agency for Drugs and Technologies in Health, 2013. Optimal care of chronic, non-healing, lower extremity wounds: a review of clinical evidence and guidelines. Ott. on, Can..

Casciari, J.J., Sotirchos, S.V., Sutherland, R.M., 1992. Mathematical modelling of microenvironment and growth in EMT6/Ro multicellular tumour spheroids. Cell Prolif. 25 (1), 1–22.

Cavallo, I., Sivori, F., Mastrofrancesco, A., Abril, E., Pontone, M., Di Domenico, E.G., Pimpinelli, F., 2024. Bacterial biofilm in chronic wounds and possible therapeutic approaches. Biology 13 (2), 109.

Cole, W., Wound Care Update: Can Bioabsorbable Borate-based Glass Fibers Support Wound Healing?, URL https://lermagazine.com/article/wound-care-update-can-bioabsorbable-borate-based-glass-fibers-support-wound-healing.

Cui, Y., Wang, Y., Liu, M., Qiu, L., Xing, P., Wang, X., Ying, G., Li, B., 2017. Determination of glucose deficiency-induced cell death by mitochondrial ATP generation-driven proton homeostasis. J. Mol. Cell Biology 9 (5), 395–408.

Dallon, J.C., Sherratt, J.A., 1998. A mathematical model for fibroblast and collagen orientation. Bull. Math. Biol. 60 (1), 101–129.

Dallon, J.C., Sherratt, J.A., Maini, P.K., 1999. Mathematical modelling of extracellular matrix dynamics using discrete cells: fiber orientation and tissue regeneration. J. Theoret. Biol. 199 (4), 449–471.

Dallon, J.C., Sherratt, J.A., Maini, P.K., 2001. Modeling the effects of transforming growth factor-β on extracellular matrix alignment in dermal wound repair. Wound Repair Regen. 9 (4), 278–286.

Dari, S., Fadai, N.T., O'Dea, R.D., 2023. Modelling the effect of matrix metalloproteinases in dermal wound healing. Bull. Math. Biol. 85 (10), 96.

Day, R.M., 2005. Bioactive glass stimulates the secretion of angiogenic growth factors and angiogenesis in vitro. Tissue Eng. 11 (5–6), 768–777.

Day, R.M., Boccaccini, A.R., Shurey, S., Roether, J.A., Forbes, A., Hench, L.L., Gabe, S.M., 2004. Assessment of polyglycolic acid mesh and bioactive glass for soft-tissue engineering scaffolds. Biomaterials 25 (27), 5857–5866.

Doorbar, J., Zheng, K., Aiyenuro, A., Yin, W., Walker, C.M., Chen, Y., Egawa, N., Griffin, H.M., 2021. Principles of epithelial homeostasis control during persistent human papillomavirus infection and its deregulation at the cervical transformation zone. Curr. Opin. Virol. 51, 96–105.

Franks, S.J., Ward, J.P., Tindall, M.J., King, J.R., Curtis, A., Evans, G.S., 2008. A mathematical model of the in vitro keratinocyte response to chromium and nickel exposure. Toxicol. Vitr. 22 (4), 1088–1093.

Gao, W., Jin, W., Li, Y., Wan, L., Wang, C., Lin, C., Chen, X., Lei, B., Mao, C., 2017. A highly bioactive bone extracellular matrix-biomimetic nanofibrous system with rapid angiogenesis promotes diabetic wound healing. J. Mater. Chem. B 5 (35), 7285–7296.

Greenhalgh, D.G., 1998. The role of apoptosis in wound healing. Int. J. Biochem. & Cell Biology 30 (9), 1019–1030.

Guest, J.F., Fuller, G.W., Vowden, P., 2020. Cohort study evaluating the burden of wounds to the UK's national health service in 2017/2018: update from 2012/2013. BMJ Open 10 (12), e045253.

Guo, X., Song, G., Li, Y., Zhao, L., Wang, J., 2022. Switch of bacteria community under oxygen depletion in sediment of bohai sea. Front. Mar. Sci. 9, 833513.

Haugh, J.M., 2006. Deterministic model of dermal wound invasion incorporating receptor-mediated signal transduction and spatial gradient sensing. Biophys. J. 90 (7), 2297–2308.

Hoppe, A., Güldal, N.S., Boccaccini, A.R., 2011a. A review of the biological response to ionic dissolution products from bioactive glasses and glass-ceramics. Biomaterials 32 (11), 2757–2774.

Hoppe, A., Guldal, N.S., Boccaccini, A.R., 2011b. A review of the biological response to ionic dissolution products from bioactive glasses and glass-ceramics. Biomaterials (ISSN: 0142-9612) 32 (11), 2757–2774.

James, G.A., Swogger, E., Wolcott, R., Pulcini, E.d., Secor, P., Sestrich, J., Costerton, J.W., Stewart, P.S., 2008. Biofilms in chronic wounds. Wound Repair Regen. 16 (1), 37–44.

Jones, J.R., 2013. Review of bioactive glass: from hench to hybrids. Acta Biomater. 9 (1), 4457–4486.

Jung, S., Day, T., Boone, T., Buziak, B., Omar, A., 2019. Anti-biofilm activity of two novel, borate based, bioactive glass wound dressings. Biomed. Glas. 5 (1), 67–75.

Kaya, S., Cresswell, M., Boccaccini, A.R., 2018. Mesoporous silica-based bioactive glasses for antibiotic-free antibacterial applications. Mater. Sci. Eng.: C 83, 99–107.

Kerr, M., 2011. Inpatient Care for People with Diabetes: The Economic Case for Change. Tech. rep., Insight Health Economics, London: NHS Diabetes.

Lansdown, A.B.G., 2002. Calcium: a potential central regulator in wound healing in the skin. Wound Repair Regen. 10 (5), 271–285.

Łapa, A., Cresswell, M., Campbell, I., Jackson, P., Goldmann, W.H., Detsch, R., Parsons, A., Ahmed, I., Boccaccini, A.R., 2019. Ga and Ce ion-doped phosphate glass fibres with antibacterial properties and their composite for wound healing applications. J. Mater. Chem. B 7 (44), 6981–6993.

Lauffenburger, D.A., Kennedy, C.R., 1983. Localized bacterial infection in a distributed model for tissue inflammation. J. Math. Biol. 16 (2), 141–163.

Liarte, S., Bernabé-García, A., Nicolás, F.J., 2020. Human skin keratinocytes on sustained TGF-β stimulation reveal partial EMT features and weaken growth arrest responses. Cells 9 (1), 255.

Lin, C., Mao, C., Zhang, J., Li, Y., Chen, X., 2012. Healing effect of bioactive glass ointment on full-thickness skin wounds. Biomed. Mater. 7 (4), 045017.

Machado, M.J.C., Watson, M.G., Devlin, A.H., Chaplain, M.A.J., McDougall, S.R., Mitchell, C.A., 2011. Dynamics of angiogenesis during wound healing: a coupled in vivo and in silico study. Microcirculation 18 (3), 183–197.

Macioch, T., Sobol, E., Krakowiecki, A., Mrozikiewicz-Rakowska, B., Kasprowicz, M., Hermanowski, T., 2017. Health related quality of life in patients with diabetic foot ulceration—translation and polish adaptation of diabetic foot ulcer scale short form. Health Qual. Life Outcomes 15, 1–8.

MacLeod, A.S., Mansbridge, J.N., 2016. The innate immune system in acute and chronic wounds. Adv. Wound Care 5 (2), 65–78.

Maheswary, T., Nurul, A.A., Fauzi, M.B., 2021. The insights of microbes' roles in wound healing: A comprehensive review. Pharmaceutics 13 (7), 981.

Maleki, H., Mathur, S., Klein, A., 2020. Antibacterial ag containing core-shell polyvinyl alcohol-poly (lactic acid) nanofibers for biomedical applications. Polym. Eng. Sci..

Mao, C., Lin, C., Chen, X., 2014. Enhanced healing of full-thickness diabetic wounds using bioactive glass and yunnan baiyao ointments. J. Wuhan Univ. Technology-Mater. Sci. Ed. 29 (5), 1063–1070.

Margolis, D.J., 2013. Epidemiology of wounds. Meas. Wound Heal.: Sci. Pr. 145–153.

McDougall, S., Dallon, J., Sherratt, J., Maini, P., 2006. Fibroblast migration and collagen deposition during dermal wound healing: mathematical modelling and clinical implications. Philos. Trans. R. Soc. A: Math. Phys. Eng. Sci. 364 (1843), 1385–1405.

in Medicine Study Group, Mathematics, 2001. Maggots: Mathematics-in-Medicine Study Group Report. Tech. rep., University of Nottingham, Nottingham, UK, URL https://mmsg.mathmos.net/uk/2001/maggots/report.pdf, (Accessed 14 August 2025).

Menon, S.N., Flegg, J.A., McCue, S.W., Schugart, R.C., Dawson, R.A., McElwain, D.L.S, 2012. Modelling the interaction of keratinocytes and fibroblasts during normal and abnormal wound healing processes. Proc. R. Soc. B: Biological Sci. 279 (1741), 3329–3338.

Metcalf, D.G., Bowler, P.G., 2013. Biofilm delays wound healing: a review of the evidence. Burn. & Trauma 1 (1), 2321–3868.

Naseri, S., Lepry, W.C., Nazhat, S.N., 2017. Bioactive glasses in wound healing: hope or hype? J. Mater. Chem. B 5 (31), 6167–6174.

Norris, E., Ramos-Rivera, C., Poologasundarampillai, G., Clark, J.P., Ju, Q., Obata, A., Hanna, J.V., Kasuga, T., Mitchell, C.A., Jell, G., 2020. Electrospinning 3D bioactive glasses for wound healing. Biomed. Mater. 15 (1), 015014.

Olsen, L., Maini, P.K., Sherratt, J.A., Marchant, B., 1998. Simple modelling of extracellular matrix alignment in dermal wound healing I. Cell flux induced alignment. Comput. Math. Methods Med. 1 (3), 175–192.

Olsen, L., Sherratt, J.A., Maini, P.K., Arnold, F., 1997. A mathematical model for the capillary endothelial cell-extracellular matrix interactions in wound-healing angiogenesis. Math. Med. Biology: A J. the IMA 14 (4), 261–281.

Pastar, I., Balukoff, N.C., Sawaya, A.P., Vecin, N.M., Tomic-Canic, M., 2024. Physiology and pathophysiology of wound healing in diabetes. In: The Diabetic Foot: Medical and Surgical Management. Springer, pp. 109–134.

Paterson, T.E., Bari, A., Bullock, A.J., Turner, R., Montalbano, G., Fiorilli, S., Vitale-Brovarone, C., MacNeil, S., Shepherd, J., 2020. Multifunctional copper-containing mesoporous glass nanoparticles as antibacterial and proangiogenic agents for chronic wounds. Front. Bioeng. Biotechnol. 8, 246.

Percival, S.L., Hill, K.E., Williams, D.W., Hooper, S.J., Thomas, D.W., Costerton, J.W., 2012. A review of the scientific evidence for biofilms in wounds. Wound Repair Regen. 20 (5), 647–657.

Pettet, G.J., Byrne, H.M., McElwain, D.L.S., Norbury, J., 1996. A model of wound-healing angiogenesis in soft tissue. Math. Biosci. 136 (1), 35–63.

Poologasundarampillai, G., Obata, A., Electrospun bioactive glass and organic-inorganic hybrid fibers for tissue regeneration and drug delivery. In: Electrospun Polymers and Composites. Elsevier, pp. 77–110.

Poologasundarampillai, G., Wang, D., Li, S., Nakamura, R., Lee, P.D., Stevens, M.M., McPhail, D.S., Kasuga, T., Jones, J.R., 2014. Cotton-wool-like bioactive glasses for bone regeneration. Acta Biomater. 10 (8), 3733–3746.

Puca, V., Marulli, R.Z., Grande, R., Vitale, I., Niro, A., Molinaro, G., Prezioso, S., Muraro, R., Di Giovanni, P., 2021. Microbial species isolated from infected wounds and antimicrobial resistance analysis: Data emerging from a three-years retrospective study. Antibiotics 10 (10), 1162.

Raziyeva, K., Kim, Y., Zharkinbekov, Z., Kassymbek, K., Jimi, S., Saparov, A., 2021. Immunology of acute and chronic wound healing. Biomolecules 11 (5), 700.

Richmond, N.A., Maderal, A.D., Vivas, A.C., 2013. Evidence-based management of common chronic lower extremity ulcers. Dermatol. Ther. 26 (3), 187–196.

Rousselle, P., Braye, F., Dayan, G., 2019. Re-epithelialization of adult skin wounds: Cellular mechanisms and therapeutic strategies. Adv. Drug Deliv. Rev. 146, 344–365.

Schugart, R.C., Friedman, A., Zhao, R., Sen, C.K., 2008. Wound angiogenesis as a function of tissue oxygen tension: a mathematical model. Proc. Natl. Acad. Sci. 105 (7), 2628–2633.

Shankaran, V., Brooks, M., Mostow, E., 2013. Advanced therapies for chronic wounds: NPWT, engineered skin, growth factors, extracellular matrices. Dermatol. Ther. 26 (3), 215–221.

Sherratt, J.A., Murray, J.D., 1990. Models of epidermal wound healing. Proc. R. Soc. Lond. [Biol] 241 (1300), 29–36.

Shirgill, S., 2024. Unravelling the Effect of Metal Ions Leaching from Bioactive Glasses on Wound Associated Biofilms. A Doctoral Thesis.

Shirgill, S., Poologasundarampillai, G., Jabbari, S., Ward, J., Kuehne, S.A., 2023. Silver-doped bioactive glass fibres as a potential treatment for wound-associated bacterial biofilms. Biofilm 5, 100115.

Simpson, M.J., Lo, K., Sun, Y., 2017. Quantifying the roles of random motility and directed motility using advection-diffusion theory for a 3T3 fibroblast cell migration assay stimulated with an electric field. BMC Syst. Biology 11, 1–9.
Stevens, D.L., Bryant, A.E., 2017. Necrotizing soft-tissue infections. N. Engl. J. Med. 377 (23), 2253–2265.
Tomasova, L., Guttenberg, Z., Hoffmann, B., Merkel, R., 2019. Advanced 2D/3D cell migration assay for faster evaluation of chemotaxis of slow-moving cells. PLoS One 14 (7), e0219708.
Traversa, B., Sussman, G., 2001. The role of growth factors, cytokines and proteases in wound management. Prim. Intent.: Aust. J. Wound Manag. 9 (4), 161–167.
Valero, C., Javierre, E., García-Aznar, J.M., Gómez-Benito, M.J., 2013. Numerical modelling of the angiogenesis process in wound contraction. Biomech. Model. Mechanobiol. 12, 349–360.
Vermolen, F.J., Javierre, E., 2012. A finite-element model for healing of cutaneous wounds combining contraction, angiogenesis and closure. J. Math. Biol. 65, 967–996.
Vesperini, D., Montalvo, G., Qu, B., Lautenschläger, F., 2021. Characterization of immune cell migration using microfabrication. Biophys. Rev. 13, 185–202.
Waugh, H.V., Sherratt, J.A., 2006. Macrophage dynamics in diabetic wound dealing. Bull. Math. Biol. 68 (1), 197–207.
Wilkinson, H.N., Iveson, S., Catherall, P., Hardman, M.J., 2018. A novel silver bioactive glass elicits antimicrobial efficacy against pseudomonas aeruginosa and staphylococcus aureus in an ex vivo skin wound biofilm model. Front. Microbiol. 9, 1450.
Wolcott, R.D., Rhoads, D.D., 2008. A study of biofilm-based wound management in subjects with critical limb ischaemia. J. Wound Care 17 (4), 145–155.
Yu, D.G., Zhou, J., Chatterton, N.P., Li, Y., Huang, J., Wang, X., 2012. Polyacrylonitrile nanofibers coated with silver nanoparticles using a modified coaxial electrospinning process. Int. J. Nanomedicine 7, 5725.
Zhao, S., Li, L., Wang, H., Zhang, Y., Cheng, X., Zhou, N., Rahaman, M.N., Liu, Z., Huang, W., Zhang, C., 2015. Wound dressings composed of copper-doped borate bioactive glass microfibers stimulate angiogenesis and heal full-thickness skin defects in a rodent model. Biomaterials 53, 379–391.